Title: Radiation-resistant binary solid solutions via vacancy trapping on solute clusters

Authors: C. Daniels, P. Bellon, R. S. Averback

Abstract:

Additions of solute that trap vacancies slow down vacancy diffusion and promote point-defect recombination in alloys subjected to irradiation. Such selective alloying can thus help to minimize the detrimental consequences resulting from point defect fluxes. The current work investigates the effect of solute additions on the recombination rate using kinetic Monte Carlo simulations for a model alloy system, which was parametrized to Cu-Ag in the dilute limit, but with an increased solubility limit, ≈ 0.86 at.% at 300K. As the solute concentration was increased above 0.1 at.%, solute clustering was observed and led to a strong increase in recombination rate. The beneficial effects of solute clustering on reducing vacancy mobility, and reducing solute drag, were analyzed by calculating relevant transport coefficients using the KineCluE code (T. Schuler et al., Computational Materials Science (2020) **172**, 109191). Moreover, it was observed in the KMC simulations that large recombination rates resulted in a shift of steady-state distributions of solute cluster sizes to smaller clusters compared to equilibrium distributions in the solid solution. This shift is rationalized as resulting from the irreversible character of the interstitial-vacancy recombination reaction. These results suggest a novel irradiation effect on phase stability where a high recombination rate increases the solubility limit of a solute at steady state over its equilibrium value.

Corresponding author: C. Daniels

Keywords: irradiation, solute-defect trapping, KMC, cluster transport

1 INTRODUCTION

The design of future nuclear reactors requires the development of structural alloys that can withstand large irradiation doses and operate safely over a wide range of irradiation temperatures [1]. A major contribution to radiation damage in nuclear structural materials derives from long-range diffusion of point defects and defect clusters to sinks, as it leads to swelling and creep at high doses, and to radiation-induced segregation (RIS) and precipitation (RIP) owing to the kinetic coupling between chemical species and point defects, see refs. [2, 3] for recent reviews on these topics. While these issues have been long recognized and intensely studied over the past several decades, finding new materials that can better withstand the extreme environments anticipated for advanced reactors remains a major challenge to the nuclear industry.

Two principal strategies have been traditionally considered to suppress radiation damage. The first seeks to introduce a high density of unbiased sinks into the microstructure, e.g., grain boundaries (GBs) and hetero-interfaces, to reduce the diffusion distances to sites where point defects can be eliminated [4]. The second approach relies on providing a high density of point-defect traps to increase point defect supersaturations and thus promote point-defect recombination [5-7]. Both approaches have shown some success, for instance the use of nanolaminates with tailored interfaces [8-10] and nanoprecipitates in oxide dispersion-strengthened steels [4] in the first approach, or the addition of oversized solutes in the second approach [11-14]. A common limitation in both approaches, however, is that the evolution of the microstructure during irradiation may remove the sinks and traps introduced during processing and result in the progressive loss of radiation resistance.

The present work focuses on the second approach. The first question is how to select the best solutes for a given matrix. The ideal solute should possess two properties: It should be an effective trap for point defects, and it should not be susceptible to solute drag by defect fluxes, otherwise the beneficial effects will disappear over time as solute is removed from solution and accumulates at sinks. Earlier works by Mansur et al. [6, 7] focused on selecting solutes that trap vacancies or interstitials. Since vacancies are generally far less mobile than interstitial atoms, they require smaller binding energies for a given goal, e.g., achieving a given reduction in swelling rate. Following works thus considered oversized solutes as they tend to correlate with a larger solute-vacancy binding energy. Kato et al. [11, 15, 16], for example, showed experimentally that such oversized solutes as Zr, Hf and Pt in 316 austenitic stainless steels (316 SS) improved radiation resistance during irradiation with 1 MeV electrons. In particular, these solute additions were effective in suppressing radiation-induced depletion of Cr at GBs. Hackett et al. [13, 14] similarly investigated the efficacy of Zr and Hf in 316 SS by contrasting the microstructural evolution under 2 and 3.2 MeV proton irradiation at 400˚C and 500˚C of a reference 316 stainless steel with that of 316 SS doped with ≈ 0.04 wt.% to 0.4 wt.% solute. They also observed that Zr addition was particularly effective in suppressing Cr-depletion at GBs. For proton irradiation at 400˚C, for instance, Cr depletion at GBs in the Zr-bearing alloys was greatly reduced compared to that in a reference 316 steel at the damage level of 3 displacement per atom (dpa). This benefit, however, disappeared at higher damage levels if the Zr concentration was low. At 7 dpa, for instance, Cr GB segregation (depletion) was -6.2±0.8 at.% in an alloy with a Zr concentration of 0.19 at.%, thus statistically identical to the depletion measured in the reference steel, -6.1±0.6 at.%. In contrast,

Cr depletion at GBs was only -4.7±0.6 at.% for a Zr concentration of 0.28 at.%. Atom probe tomography showed that some of the added solute had been removed from solution at those higher doses, and it was proposed that this solute removal resulted from the diffusion of Zr and Hf and their incorporation into pre-existing precipitates, e.g., ZrC and HfC. To better understand the loss of solute in irradiated alloys, Schuler et al. developed a continuum kinetic model to quantify the rate of solute removal from an infinitely dilute solid solution arising from solute drag and its impact on point defect recombination [17]. In this model, defect and transport coefficients are calculated based on the self-consistent mean-field (SCMF) approximation [18-20], using point defect jump frequencies obtained by first principles calculations. The transport coefficient formalism was later generalized in the recently released KineCluE code [21]. Schuler's model indicates that for effective trapping at temperature T the solute-vacancy binding energy, E_b must $E_b \gtrsim 3\ k_B T$ [22]. For instance, the application of the model to a dilute Cu-Sb alloy revealed that isolated Sb solute atoms, which have a calculated binding energy to a vacancy of 0.38 eV, could effectively trap vacancies up to ≈ 1000 K [22]. Because of a strong solute-vacancy flux coupling in that system, however, most Sb atoms would be removed from solution in less than 1 dpa at temperatures ≲ 500 K [17]. In moderately dilute alloys, however, this limitation may not be so severe since solute atoms will be at sufficiently high concentrations to begin interacting with one another, and if properly selected, they will form less-mobile clusters, as we discuss next.

The combined effects of solute clustering on point defect trapping, solute drag and recombination, to the best of our knowledge, have not been systematically investigated but it is clear that solute clusters could be highly beneficial. For example, solute clustering will increase the trapping strength since vacancies trapped on a cluster can bind to multiple solute atoms [23], thus pushing to higher temperatures the range of effective trapping. First-principles calculations in dilute Fe-X alloys [24], for instance, indicate that the binding energy for a complex comprised of one vacancy bound to *n* solute atoms, designated here as VX_n, increases from 0.27 eV, to 0.54 eV, to 1.06 eV, and to 1.47 eV for n = 1, 2, 3, and 4 for X = Cu (note that the VX_n notation is used when the reference state is the one where all the members of the cluster are dissociated; in contrast, $V\text{-}X_n$ refers to the binding energy of a vacancy to a bound complex of *n* solute atoms, following the notation used in [25]). Furthermore, clustering of the point defects themselves on a single solute atom can also increase trapping, as illustrated by first-principles calculations in dilute Fe-Au alloys [25]: While the binding energy of a single vacancy to a Au solute is 0.38 eV, it increases to 0.88 eV for a divacancy. Combined positron annihilation and TEM characterization of $Fe_{99}Cu_1$ and $Fe_{99}Au_1$ alloys after irradiation with He ions at 550 ˚C has in fact showed that Au provided a greater increase in resistance to swelling than Cu, owing to its higher binding energies for $V_m\text{-}Au_1$ and $V_m\text{-}He_m\text{-}Au_1$ clusters compared to $V_m\text{-}Cu_1$ and $V_m\text{-}He_m\text{-}Cu_1$ clusters [25]. A second effect of solute clustering is that it will modify solute transport. While large solute clusters are expected to be less mobile than single solute atoms [26], in some alloy systems, e.g., Fe-Cu, atomistic simulations predict that the solute cluster mobility first increases with size at small cluster sizes, before decreasing with size as they grow larger [27]. In this work we consider a model immiscible alloy system based on the properties of Cu-Ag to investigate the effect of solute concentration and clustering on point defect recombination during irradiation using kinetic Monte Carlo (KMC) simulations. The alloy model and the simulation parameters are introduced in Section 2. The results, presented in Section 3, indicate that solute clustering is indeed very effective in promoting recombination as well as in reducing solute drag. These results, and an intriguing new finding that the recombination reaction can affect phase stability, are discussed in Section 4.

2 METHODS

2.1 ENERGETICS AND KINETICS

For the present study, the binary A-B alloy on a rigid face centered cubic (FCC) lattice previously introduced in ref. [23] is selected. The main components of the model are briefly summarized here, but additional details can be found in ref. [23]. The energy of a configuration is modeled as the sum of pairwise interactions ε_{ij} between 1st nearest neighbor (NN) sites occupied by species i and j (i, j = A, B, V). The corresponding equilibrium phase diagram is determined by the ordering energy $\omega = 2\varepsilon_{AB} - (\varepsilon_{AA} + \varepsilon_{BB})$. The ordering energy is positive, i.e., corresponding to an alloy with a tendency toward phase separation, which results in solute clustering when the solute B concentration approaches its solubility limit. Appendix A provides the equations relating the ε_{ij}'s and ε_{BB} to physical quantities such as cohesive energies and vacancy formation energies. An important quantity in this work is the binding energy between vacancy and solute, defined as the energy difference between unbound and bound (1st NN) states, i.e., $E_b = (\varepsilon_{AB} - \varepsilon_{AA}) + (\varepsilon_{AV} - \varepsilon_{BV})$. With this definition, a positive binding energy corresponds to an attractive interaction between the solute B and vacancies.

Thermally activated diffusion is modeled using the broken-bond model as defined in refs. [28, 29]. Specifically, the energy barrier for a vacancy jump is calculated as a saddle point energy contribution for that jump type minus the sum of the vacancy-atom interactions of the nearest neighbors and the atom-atom interactions of the atom the vacancy is replacing. In the dilute limit and with only 1st NN interactions, there are five distinct jump frequencies to consider [30, 31]. Following the standard notation, these jumps correspond to a vacancy moving through the matrix (w_0), hopping around a NN solute (w_1), exchanging with a solute (w_2), and disassociating from (w_3) or associating with (w_4) a solute. Each of these jumps has a corresponding activation energy barrier (E_i). Since the association and dissociation jumps are reversed jumps from one another and share the same saddle point energy, the binding energy can be calculated as $E_b = E_3 - E_4$.

This alloy system is closely related to Cu-Ag. Specifically, for an infinitely dilute alloy all the parameters are fitted to the DFT values obtained by Wu et al. for Cu-Ag for the standard five jump frequencies [32, 33]. Four distinct saddle point energy contributions, S_i, are used to fit these 5 activation energies. As detailed in our previous work with this parametrization for the infinitely dilute system [23], the resulting solute-vacancy binding energy is $E_b = 0.115$ eV, and it is therefore anticipated that, at infinite dilution, the maximum trapping temperature would be ≈ 450 K using the rule given in the Introduction that $E_b \gtrsim 3\, k_B T$. Furthermore, the ratio w_3/ w_1 is large, thus at low temperature, a vacancy flux will induce a solute flux in the same direction, resulting in solute drag as opposed to an inverse Kirkendall effect, which requires that w_3/ w_1 be small. Using the criteria $E_o - E_4 \gtrsim 3k_B T$ identified for solute drag in ref. [17], solute drag is expected to take place at temperatures below ≈ 500 K since $E_o - E_4 = 0.128\, eV$, and, conversely, inverse Kirkdendall effect is expected above that temperature. These expectations will be confirmed by calculations of solute drag ratios presented in Section 3.4.

For non-infinitely dilute alloys, there are more than 5 independent jump frequencies owing to the presence of multiple solute atoms, but at concentrations small enough for solute clusters to remain isolated, the corresponding jump frequencies can be grouped into families of w_1-type, w_2-type, w_3-type, and w_4-type jumps based on the nature of the jumping atom and the effect on the configuration. In order to minimize the number of unknown and adjustable parameters, the same 4 saddle point energies S_i defined for infinite dilution are re-used here. The following rules are used to assign any jump to one of those 4 families, and thus to select a particular S_i value: (i) any A-V exchange where there are no B 1st NN to the vacancy before and after the exchange is an w_0 jump; (ii) any B-V exchange is a w_2-type jump; (iii) any A-V exchange for which there are some B atoms in the 4-atom saddle point window of an FCC crystal is considered as a w_1-type jump; and lastly (iv) any other A-V exchange for which there are no B atoms in the 4-atom saddle point window is considered as w_3/w_4-type jump. These simplified rules capture the trends of the dependence of the vacancy activation energy with local chemical environments determined for small solute clusters by molecular statics calculations in LAMMPS using the Williams-Mishin-Hamilton Cu-Ag potential [34], see Appendix A. Although improved agreement between activation energies calculated by the pairwise interaction model and the Williams-Mishin-Hamilton potential could be obtained using, for instance, composition-dependent saddle-point energies as in Ref. [27], no such attempt was made here, primarily because the present study focuses on a modified Cu-Ag model, for reasons detailed in the next paragraph.

The one alloy parameter that is not fitted to the actual Cu-Ag system is the ordering energy, which has been adjusted so as to increase the solubility limit at low temperature [23]. This modification was motivated by the relatively small vacancy binding energy with Ag solute in Cu, 0.11eV, and thus vacancy trapping is only expected to be significant below ~ 400 K. At these low temperatures, Cu and Ag are almost completely immiscible. The solubility of Ag in Cu in the model was thus increased by reducing the critical temperature of the miscibility gap, T_c, from an estimated value of 1200 K to 600 K; this was accomplished by adjusting ε_{AB}. This shifts the solubility limit at 300 K from < 0.1 at.% for actual Cu-Ag to 0.86 at.% ± 0.05 at.% for our model alloy, as determined using semi-grand-canonical equilibrium MC simulations. We refer here to this alloy parametrization as "modified Cu-Ag alloy". The physical input values are listed in Table 1, while the resulting interaction energies and saddle points used in this study are listed in Table 2. The only difference with the parameters used in ref. [23] is that the (constant) vacancy attempt frequency is set to 3.41×10^{12} s^{-1} to match the DFT data for infinitely dilute solute concentration.

Table 1 Input parameters used to generate the modified Cu-Ag parameterization. See Appendix A for full equations.

E_{coh}^{A}	E_{Vf}^{A}	E_0	E_1	E_2	E_3	E_4	E_{coh}^{B}	T_c(K)
-3.49	1.28	0.7174	0.9040	0.5785	0.7047	0.5895	-3.174	600K

Table 2 KMC simulation parameters corresponding to Table 1. S_i refers to the saddle-point energy contribution of the i-type jump, with index i referring to the 5-frequency notation.

ε_{AA}	ε_{AV}	ε_{AB}	ε_{BB}	ε_{BV}	S_0	S_1	S_2	$S_{3,4}$

-0.582	-0.184	-0.545	-0.529	-0.263	-7.891	-7.746	-7.702	-7.982

2.2 IRRADIATION EFFECTS

Single Frenkel pairs are introduced on sites randomly selected from those occupied by A atoms at a rate imposed by the damage rate ϕ (in dpa/s). The simulations are therefore mostly representative of defect production during high-energy electron or proton irradiation. Results reported here were obtained for a damage rate of 10^{-6} dpa/s and an irradiation temperature of 300 K, unless specified otherwise. Once two sites have been selected, one of these sites is converted to a vacancy while the other becomes an AA dumbbell interstitial. Production of AB and BB dumbbells was not included because those dumbbells would transform to AA dumbbells after a jump or two because Ag is significantly oversized in Cu (the misfit parameter calculated from pure Cu and Ag lattice parameters is 13%). Implicit in this defect production process, is that there are no ballistic exchanges between A and B atoms, and thus the relocation of the A atom selected to form the dumbbell is the only contribution to recoil mixing; this simplification will be seen to be very useful later in this work. Once produced, defects can migrate and vacancy migration takes place as described in the previous section. Interstitial diffusion is treated in a simplified manner, which ignores the crystallographic orientation of the dumbbell and its local environment. Interstitials migrate randomly in space by moving one of the two components of the dumbbell interstitial to a NN site with a single, rapid jump frequency of 3.21×10^{11} s^{-1} at 300 K. Interstitials can migrate through the whole configuration, including solute rich regions, i.e., mixed dumbbells are allowed, but only A atoms are permitted to migrate. This simplified interstitial migration model is thus equivalent to a direct interstitial mechanism restricted to A atoms only. This choice is motivated by two considerations. First, as already indicated above, Ag is significantly oversized in Cu and prior works indicate that oversized solute atoms do not couple with interstitial fluxes [35-38]. Second, the attractive interactions between solute atoms and vacancies will lead to their co-clustering, as detailed later in Section 3. If only AA dumbbells were allowed, vacancies completely surrounded by B atoms would rarely recombine and solute-enriched regions, for instance near the sink plane, could form an obstacle for interstitial diffusion. The simplified interstitial migration model used here ensures that there is no solute drag by interstitials while avoiding the unwanted effects of solute-rich regions on interstitial migration.

As defects migrate through the system, they are removed either through recombination or absorption at the sink. A vacancy and interstitial will immediately recombine if they diffuse within three 1st NN spacings of each other with the vacancy being filled by a randomly selected component of the interstitial. This recombination radius approximates the recombination volume of 125 Ω_0 measured for Cu [39], Ω_0 denoting the atomic volume. The sink is a single (111) plane that absorbs all vacancies and interstitials immediately after they reach the sink, using a reservoir as in ref. [28], so that the atom number need not be conserved.

Two additional simplifications were made regarding irradiation effects. First, since a pairwise interaction model becomes challenging to parametrize when vacancies form clusters, the system was prevented from forming di-vacancies through either vacancy jumps or defect production. Note

that for the system size and parameters used in this study there is at most one interstitial present in the computational cell at any given time, and thus there is no need to consider interstitial clustering. Secondly, as indicated earlier, the ballistic mixing due to the forced replacement of A atoms (resp. B atoms) by B atoms (resp. A atoms) in replacement collision sequences and displacement cascades was not included in the model, so as to isolate the microstructural effects arising from thermally activated migration of point defects and their recombination and elimination on the sink plane. The consequences of these simplifications on the KMC results are discussed in Section 4.

2.3 LATTICE KINETIC MONTE CARLO SIMULATIONS

For all simulations in this study, a rhombohedral simulation cell is used, which consists of 128×128 atoms in (111) planes parallel to the sink plane, with 3 different values for the number of planes (including the sink plane): 48, 86 and 152, which correspond respectively to sink separation distance t of 10.0 nm, 17.9 nm and 31.7 nm in pure Cu. These values were selected to cover a range of sink strengths. Using the geometric definition of sink strength for a thin foil, $k^2 = \pi^2/t^2$, [40, 41], the corresponding sink strength values are 9.8×10^{16} m^{-2}, 3.1×10^{16} m^{-2} and 9.8×10^{15} m^{-2}. The above sink strength values, however, do not account for point defect recombination [42, 43], the rate of which increases with solute addition as will be shown in Section 3. Recombination-dependent sink strengths are provided in Table A1 (see Appendix A) using the approach of Doan and Martin [43] and the KMC recombination rates for each alloy composition.

The system is evolved through the Equilibrating Chain KMC algorithm introduced in Ref. [23]. The algorithm is based on the standard BKL Residence Time Algorithm (RTA), also known as the 1st Order RTA [44]. The probability p_i of a given event i occurring out of j possible events is weighted by their rates r_j as $p_i = r_i/\sum_j r_j$. While the timestep is often selected from an exponential distribution, we are interested in long sequences of events and thus use the ensemble average timestep of $\Delta t = 1/\sum_j r_j$. Jump probability data is stored as the system evolves, allowing for the selective application of a 2nd order calculations in what is known as Chain KMC, which bypasses immediate reversals or 'flickers' [45]. Additionally, the system is monitored for energy basins where vacancies may be trapped and come to equilibrium. When this is found to have occurred by means of a statistical test, the vacancy is allowed to directly escape the basin on the next step. Note that this direct escape is employed only when it is statistically valid.

In order to investigate the response of the above alloy system near the onset of solute clustering, the solute concentration is varied from 0.0 to 2.0 at.% , i.e., from pure Cu used as a reference, to very dilute concentrations, typically $\lesssim 0.1\ at.\%$ to concentrations where non-dilute effects and solute clustering become significant, $\gtrsim 0.5\ at.\%$

3 RESULTS

The two main issues addressed in this study are (1) the effectiveness of the solute in promoting point-defect recombination, and the dependence of this efficacy on the initial solute concentration and irradiation dose; and (2) the potential loss of solute in the bulk due to radiation-induced solute segregation at sinks. These issues were addressed by monitoring as a function of dose, the point defect and solute concentration profiles, as well as the overall fraction of point defects that recombine, F_R. In Section 3.1, typical solute and point defect concentration evolutions with dose are presented, before analyzing in Section 3.2 the evolution of the recombined fraction with dose for various initial solute concentrations and various sink strengths. Solute clustering and its effect on F_R are then quantified in Section 3.3. Lastly, the effects of clustering on promoting recombination and suppressing solute drag are analyzed in Section 3.4, in part using the KineCluE code to complement the KMC results.

3.1 POINT DEFECT AND CONCENTRATION PROFILES.

All simulations were initialized with a random distribution of solute atoms, and at early times the evolution of the system matched closely that expected for a unary system bounded by perfect sinks. At high doses, a steady state was reached, and typical steady-state solute and vacancy concentration profiles are shown in Figs. 1(a) and 1(b), respectively. One observes the formation of solute-rich shoulders near the sink, as expected due to solute drag by the vacancy flux at low temperature. The sink plane itself is fully depleted of solute, but solute enrichment is observed on the second and third nearest planes adjacent to the sink. These features stem from the details of vacancy and solute jumps near the sink plane. For instance, if an isolated solute atom is approaching the sink as a solute-vacancy pair, the vacancy can reach the sink plane either through rotation (w_1) or dissociation (w_3) jumps, which result respectively in leaving behind its bound solute on either the 1st or 2nd planes adjacent to the sink. To quantify solute segregation on the sink, the average solute concentration is thus calculated over 4 planes, skipping the sink plane itself but including the 1st and 2nd planes on both sides of the sink. The average solute concentration on all other planes, again excluding the sink plane, is used as a measure of the bulk solute concentration. A consequence of the build-up of a solute-rich shoulder near the sink is the formation of an overlapping vacancy-rich peak, see Fig. 1(b), owing to the strong solute-vacancy binding. This vacancy peak, in turn, can increase the local recombination rate in that region. This effect, however, is found to be small for all parameters studied here, producing only a minor increase in the recombination probability near the sink, see for instance Fig. 1(c). The recombination probability is defined as the fraction of recombination events in the system filling a vacancy on a given plane, measured at steady state.

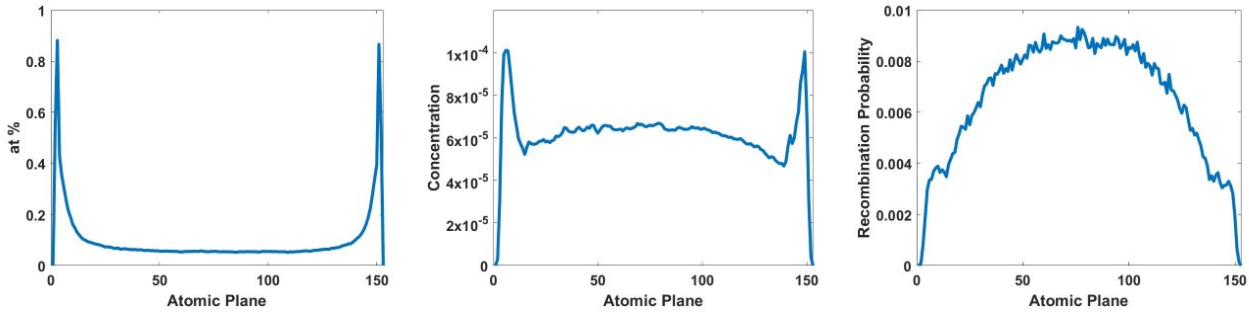

Figure 1. Steady-state profiles of (a) B solute concentration in at.%, (b) vacancy concentration and (c) recombination probability. ~~The 'recombination probability' is defined as the fraction of recombination events in the system filling a vacancy on a given plane measured at steady state~~. Initial solute concentration is $[B]_{ini}$ = 0.1 at.%; system size is 1282x152 sites; data has been averaged from 0.1 dpa to 0.2 dpa. The sink plane has zero vacancy concentration due to annihilation, and zero solute concentration due to preferential removal of solute by the vacancies and interstitial solvent drag.

3.2 EFFECT OF SOLUTE CONCENTRATION ON THE RECOMBINED FRACTION.

We now turn to the evolution of the solute concentrations at the sink and in the bulk, as well as the evolution of the recombined fraction F_R, defined as the number of point defects that recombine normalized by the number of point defects produced as Frenkel pairs. These quantities are averaged over time (i.e., dose) to reduce fluctuations, but the averaging dose intervals are kept sufficiently short, here 1×10^{-4} dpa, to retain good dose resolution at low doses. For instance, these data show that solute segregation at the sink reaches a steady state at quite small doses, e.g., ≈ 0.02 dpa at 300 K for a system size of 128^2x86 and for solute concentrations ranging from 0.01 to 0.5 at.%, see Fig. 2. Part of the reason for these quite low doses, in comparison to experiments, stems from the fact that every point defect created in these simulations is a freely migrating defect, whereas in experiments only a few percent of created defects, at most, become freely migrating [46-48]. The recombined fraction F_R, in contrast, displays very limited evolution with dose. This is because F_R is dominated by the bulk solute concentration, which does not change as significantly with dose in those cases. While the bulk solute concentration is complementary to the sink concentration, the bulk region is much larger than the sink region (about 20 times as large as the sink in Fig. 2). Thus, the relative concentration change in the matrix is much smaller, being in these cases approximately 65%, 77%, and 95% of the initial solute concentrations (0.01, 0.1, 0.5 at% respectively). Plots of the matrix concentration are provided in the Supplementary Information.

As anticipated for the present alloy, increasing the solute concentration promotes the reduction of vacancy diffusion, and therefore it results in an increase in the recombined fraction at steady state, F_R^{ss}, see Fig. 3. In the very dilute to dilute regime, up to ≈ 0.1 at.%, this increase in F_R^{ss} with solute concentration is fairly small, regardless of the sink strength. For instance, for a system size of 128^2x86, F_R^{ss}, increases from ≈ 41% for an initial solute concentration $[B]_{ini} = 10^{-3}$ at.%, to ≈ 45% for $[B]_{ini}$ = 0.1 at.%. In contrast, the increase is much larger for non-dilute alloys, i.e., for solute concentrations exceeding ≈ 0.5 at.%. For instance, for $[B]_{ini}$ = 1.0 at.%, F_R^{ss} reaches 82% for the same system size. This increase in recombination fraction, moreover, is significant for all values of the sink strength. Fig. 3 also shows that the continuum model of Schuler et al. [17], slightly modified here to match the conditions used in the KMC simulations as detailed in Appendix B, predicts an increase in F_R^{ss} with $[B]_{ini}$ that is in good agreement with

the KMC data for the dilute alloys but fails to capture the significant increase in non-dilute alloys. Note that this continuum model does not include solute clustering. Solute clustering is, however, significant in non-dilute alloys, as will be illustrated in the next section.

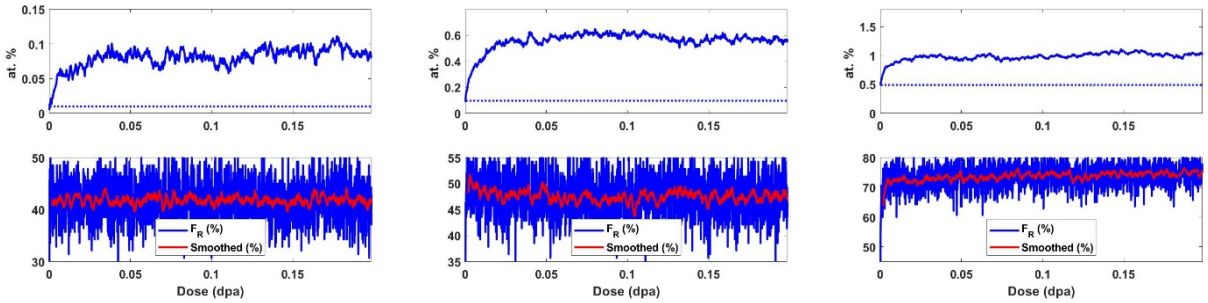

Figure 2. Plots of solute concentration at the sink (top) and recombined fraction F_R (below) as a function of dose obtained from the Equilibrating Chain KMC results for a dilute modified Cu-Ag alloy. The dotted line indicates $[B]_{ini}$. System size is 128^2x86 sites, and Ag concentration is 0.01 at.% (Left), 0.1 at.% (Center), and 0.5 at.% (Right).

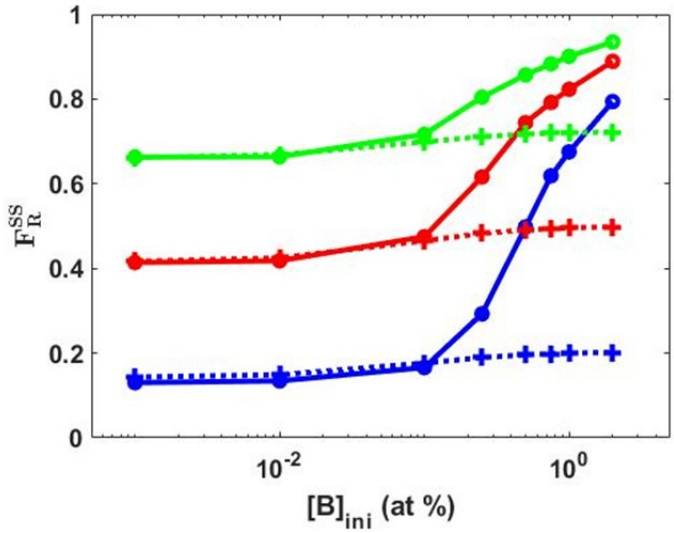

Figure 3. Evolution of the steady-state recombined fraction F_R^{SS} as a function of the initial solute concentration for three different system sizes, 128^2x152 sites (green curves), 128^2x86 sites (red curves) and 128^2x48 sites (blue curves). The "o" symbols and solid lines correspond to KMC results, while "+" symbols and dotted lines correspond to results obtained from a continuum model that only includes vacancy trapping on single solute atoms, see Appendix B. F_R^{SS} is obtained by taking the average of F_R over the [0.1,0.2] dpa dose interval. Note the dramatic increase in F_R^{SS} when the solute concentration exceeds 0.1 at%.

3.3 SOLUTE CLUSTERING DURING IRRADIATION.

At the temperature considered in the KMC simulations, 300 K, the equilibrium solubility is 0.86 at.% and therefore solute clustering is expected upon approaching or exceeding that concentration. It is well known, however, that irradiation can modify the solubility limits at steady state, namely that thermodynamic and kinetic coupling between point defects and solute atoms can promote precipitation and thus lower the solubility, while ballistic mixing can suppress precipitation and thus increase the solubility. As already indicated in Section 2, the present KMC simulations do not include ballistic exchanges between A and B atoms therefore clustering and possibly precipitation

can be expected for alloys with $[B]_{ini}$ approaching and exceeding 0.86 at.%, but these points will be discussed in detail in Section 4.

Clusters were identified in the KMC configurations as solute atoms and vacancies connected to other solute atoms or vacancies by one nearest neighbor distance. The size distributions of these clusters were determined at steady state by averaging measurements taken over the interval 0.1 to 0.2 dpa. For alloys with $[B]_{ini} < 0.1$ at.%, the vast majority of solutes and vacancies are isolated, or they form small clusters containing at most a few solutes and vacancies, as shown in Fig. 4 for a 0.1 at.% alloy. The number of vacancies in those clusters is smaller than that of solute atoms. This stems primarily from the much lower vacancy concentration compared to the solute concentration, and to a lesser extent from the constraint imposed in the KMC simulations that prevents the formation of divacancies. Closer to and near the equilibrium solubility, e.g., $[B]_{ini}$ = 0.5 at.% and $[B]_{ini}$ = 1.0 at.%, the size and the number density grew as expected, see Figs. S2-S3 (see Supplementary material). More importantly, at larger solute concentrations, $[B]_{ini}$ = 2.0 at.% in Fig. 5, i.e., well above the equilibrium solubility limit, while clustering was more pronounced, no well-defined precipitates were detected. For example, we note that the sizes of the solute clusters are smaller than the critical nucleus, which was estimated to be ≈ 7000 and ≈ 162 atoms for the 1.0 at.% and 2.0 at.% alloys respectively. This estimation was made using classical nucleation theory [49] and an average interface energy of 0.081 J/m^2 [50] as T = 300 K corresponds to a reduced temperature T/T_c=0.5. The lack of precipitation can thus be attributed to either the finite time interval employed to collect the data, or the possibility that irradiation changes the solubility limit. To test these two hypotheses, the above irradiation simulations were followed by annealing simulations at the same temperature of 300 K, starting from the last irradiation frame, keeping all the vacancies in the simulation cell, and converting the sink plane into a regular atomic plane. The one interstitial that is possibly present in the cell at the end of the irradiation can be neglected, since, if present, it would quickly recombine with a vacancy. Annealing was performed for 2×10^9 vacancy jumps, i.e., ≈ 800 vacancy jumps per atom in the cell. This represents long annealing times, especially considering the fact that these jumps are effective jumps performed by the Equilibrating Chain algorithm, and thus each effective jump may represent many (tens to millions) individual vacancy jumps. Annealing led to a pronounced increase in cluster size, as seen in the bottom rows of Figs. 4-5, and Figs. S2-S3. Moreover, vacancies are mainly found in very small solute clusters during irradiation, but in much larger solute clusters during annealing, as shown in Fig. 6. Notice that while large clusters are observed after annealing, no obvious "macroscopic" precipitates are observed after annealing for 2×10^9 vacancy jumps in the alloys containing 1.0 at.% and even 2.0 at.% solute, indicating that precipitation is very sluggish in those alloys, most likely because of the strong trapping of the vacancies on the solute clusters.

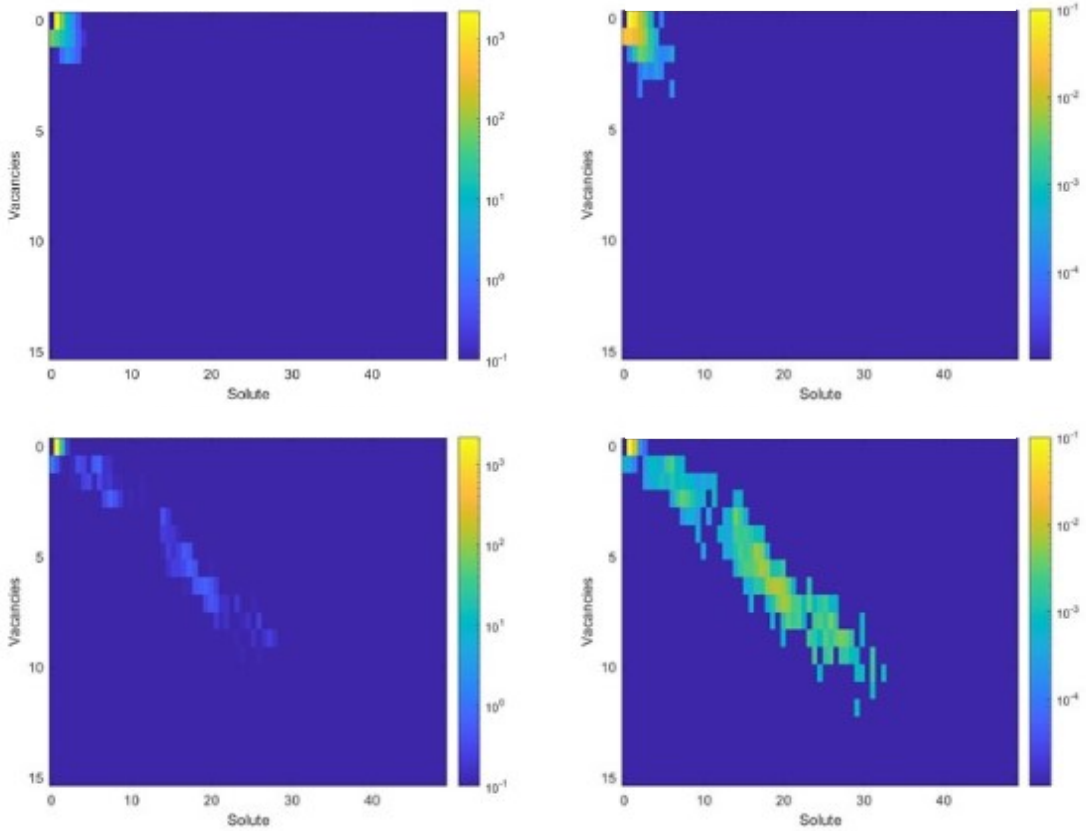

Figure 4 (Top row): Solute-vacancy clusters at steady state for a solute initial concentration is 0.1 at.%, the average vacancy concentration 6.2x10^{-5}, the system size 128^{2}×152. Left column: Histograms of clusters; Right column: Probability of clusters weighted by their volume. (Bottom row): Solute-vacancy clusters during annealing at 300 K with irradiation off (no defect production), starting from the last irradiation frame and keeping all its vacancies. Annealing is performed over 2×10^{9} vacancy jumps*, and cluster counting is done in the second half of the annealing.*

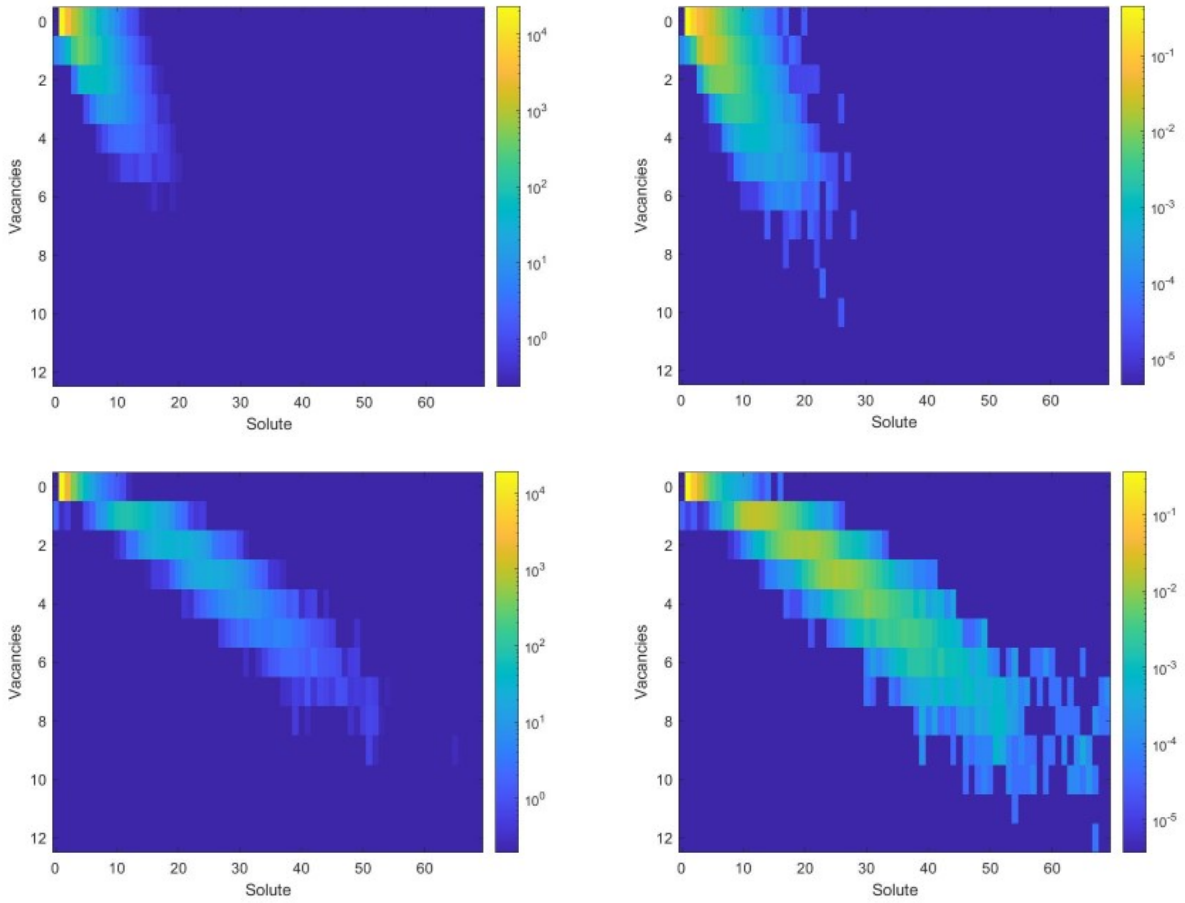

Figure 5: Same as Fig. 4 but for an initial solute concentration of 2.0 at.%*; the average steady-state vacancy concentration is* 1.0×10^{-3}.

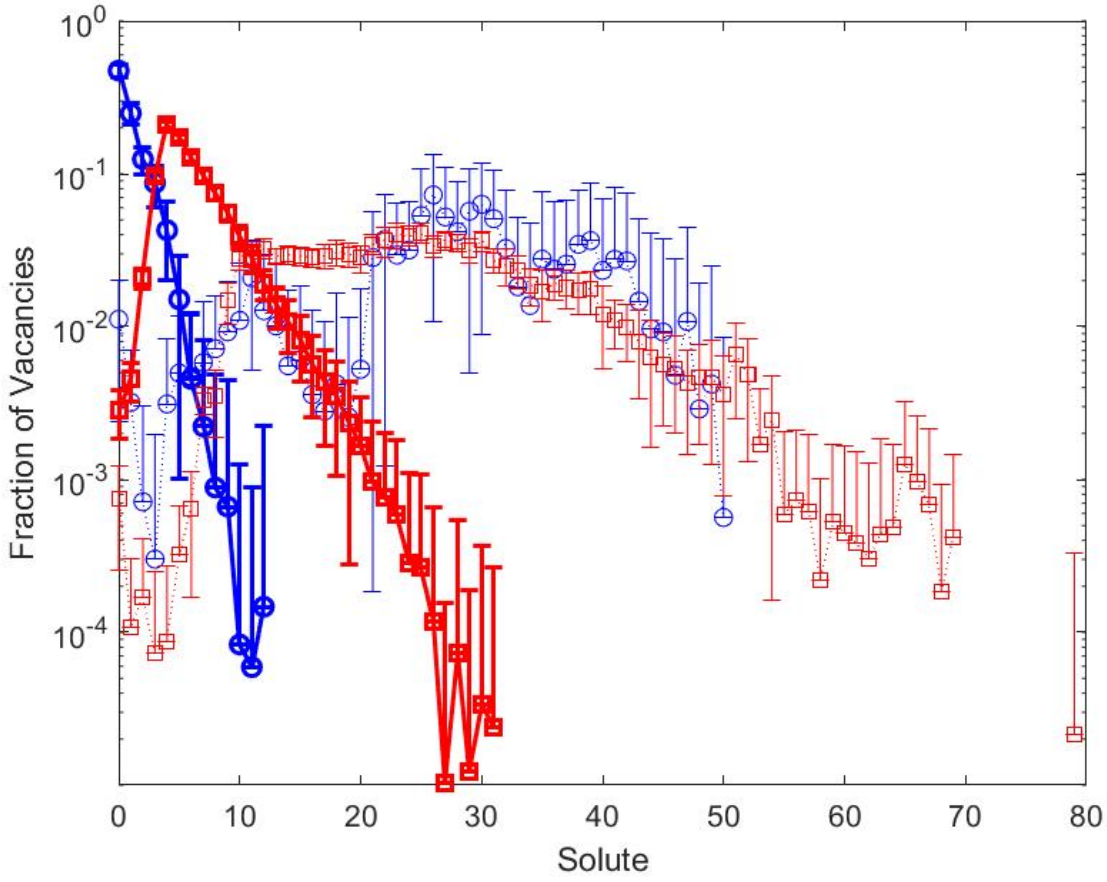

Figure 6. Fraction of vacancies in solute clusters as a function of the number of solute atoms in the clusters, calculated from the data displayed in Figs. 4 and 5. Blue and red curves correspond initial solute concentrations of 0.1 at.% and 2.0 at.%, respectively. Solid lines refer to steady-state distributions under irradiation, while dotted lines refer to distributions from the second half of the thermal annealing simulations. Error bars indicate one standard deviation. If an error bar extends below the range of the plot it is omitted for clarity.

To verify that the above irradiation results indeed correspond to steady-state configurations, irradiation was resumed after thermal annealing: Cluster sizes then became smaller, and cluster distributions returned to those measured during the first irradiation, confirming that those distributions represented true steady-states. This is illustrated in Fig. 7 using the evolution of the short-range order (SRO) parameter with dose or time. The SRO is determined by counting the number of B-B 1st NN pairs and normalizing the values so that 0 corresponds to a random solid solution and -1 to a fully decomposed state. Since solute tends to segregate to the sinks during irradiation, the overall SRO parameter is reported as well as the SRO parameter and the solute concentration from the inner half of the sample, away from the sink in order to exclude the contribution of clusters near the sinks. Both values of SRO are much more negative during annealing, indicating a stronger clustering, with the exception of the lowest solute concentration Fig. 7(a) because of a near complete vacancy depletion of the inner region. The slight differences in overall and inner SRO values for the more concentrated alloys are primarily due to minor concentration changes, as seen in Fig. 7.

From the totality of the results presented in this section, it is concluded that (i) significant solute clustering takes place in the non-dilute alloys during annealing at 300 K, i.e., $[B]_{ini} > 0.1$ at.%; (ii) irradiation suppresses clustering, and it seems to shift the solubility limit under irradiation to a value greater than that under equilibrium conditions. This novel and surprising observation will be discussed in further detail in Section 4.

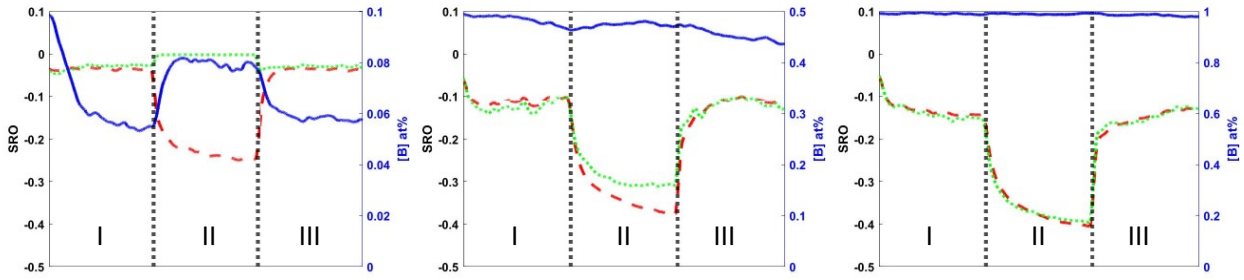

Figure 7. Evolution of the overall SRO parameter (red dashed curve), of the SRO parameter in the grain interior (green dotted curve) and of the solute concentration in the grain interior (blue curve). Initial solute concentration is (a) 0.1 at.%, (b) 0.5 at.% and (c) 1.0 at.%. The system size is $128^2 \times 152$. The first and the second irradiation steps (I and III) are for 0.2 dpa each, and the annealing step (II) is performed for 2×10^9 V jumps.

3.4 EFFECT OF SOLUTE CLUSTERING ON VACANCY MOBILITY AND SOLUTE DRAG

In our model using pairwise interactions, the binding energy of a vacancy to a solute cluster increases linearly with the number of solute neighbors. For the specific parametrization used here, the binding energy increases 0.11 eV per solute. At 300 K, the factor, $(\exp(-E_{VBn}/k_BT))$, decreases by 70.5, 5.0×10^3, and 3.5×10^5, for 1, 2, and 3 solutes, respectively. For a given cluster, however, the overall trapping is affected by all the sites a vacancy can bind to in that cluster. To quantify this overall trapping for small clusters, we determined in separate KMC simulations the time required for a vacancy to 'escape' from compact clusters comprised of 1 to 5 solute atoms and one vacancy. For simplicity, an 'escape' is defined as any vacancy exchange with a solvent atom, so it includes w_1 jumps. This choice was made because those exit times are an integral part of the Equilibrating Chain algorithm itself [23], and thus they are directly available. The true escape of a vacancy from a cluster requires the vacancy to migrate beyond the thermodynamic range of interaction; nevertheless, the cluster exit times from the Equilibrating Chain algorithm provides a useful first approximation because the effect is so strong. As can be seen in Fig. 8(a), the larger the number of solute atoms in the cluster, the longer the exit time. Furthermore, for each cluster size the temperature dependence of the exit time is well approximated by an Arrhenius law. For the single solute cluster, the activation energy for the exit time is equal to 0.7045 eV, i.e., equal to E_3, the activation energy for the w_3 vacancy jump. This is expected since for the temperature range considered here $w_3 >> w_1$ (recall that E_1=0.904 eV). For larger clusters, it is observed that the activation energy for exit increases with the cluster size. The data shown in Fig. 8(a) can in fact be fitted by assuming a single effective binding energy E_{VB}^{eff} of ≈ 0.080 eV per bound solute, as shown in Fig. 8(b). The fact that this effective binding energy is smaller than the V-B binding energy,

E_{VB}=0.11 eV, seems reasonable, as illustrated for a vacancy bound to a two-solute cluster. Instead of one w_3 jump frequency, there is now a family of exit pathways, and for some of those, the w_1 jumps are no longer negligeable. When the vacancy is bound to both solute atoms, the activation energy for a direct escape is now increased by ≈ E_{VB}, and since E_3+E_{VB}=0.820 eV the approximation w_3>>w_1 is no longer valid for the temperatures of interest. It is somewhat remarkable that a single effective binding energy can capture the temperature dependence of exit time for all the small and compact clusters considered here, but it is anticipated that such a simple scaling will not work as well for larger and less compact clusters and at higher temperatures. Returning to the effect of solute clustering on vacancy trapping, these larger binding energies have a strong effect on vacancy trapping since as solute atoms cluster, the number density of large clusters either stays constant (in a growth regime) or decreases inversely with the average cluster volume (in a coarsening regime), while the trapping strength increases as a power law with an exponent *n* equal to the number of solute in a cluster. As a consequence, as long as $E_{VB}^{eff} \gtrsim 3\, k_B T$, clustering is very effective in increasing vacancy trapping and thus in promoting point defect recombination.

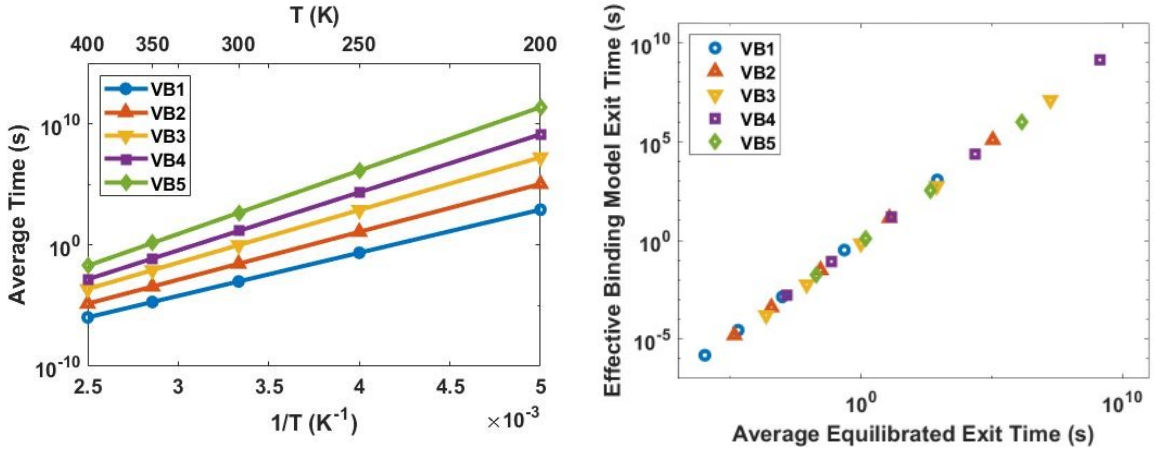

Figure 8. (a)Left: Vacancy exit time as a function of temperature measured in separate KMC simulations with cells containing a single compact cluster, containing 1 to 5 solute atoms. (b) Right: Exit times predicted assuming a single effective binding $E_{VB}^{eff} = 0.080$ *eV versus the actual exit times shown in (a).*

The effects of clustering on vacancy transport and solute drag were quantified for small clusters using the code KineCluE [21]. This method makes it possible to calculate the Onsager coefficients relating fluxes of solute and point defects to thermodynamic driving forces. For sufficiently dilute concentrations, clusters can be assumed to be at local equilibrium, and total transport coefficients can then be expressed as a sum over contributions from clusters of different size. In particular, the transport coefficient relating the flux of vacancies to the gradient in vacancy chemical potential, L_{VV}, is expressed as a sum over the contributions due to free vacancies, whose concentration is denoted by [V], vacancies bound to one solute atom, whose concentration is denoted by [VB], vacancies bound to two solute atoms, whose concentration is denoted by [VB_2], and so on:

$$L_{VV} = [V]L_{VV}^{V} + [VB]L_{VV}^{VB} + [VB_2]L_{VV}^{VB_2} \ldots \quad (1)$$

For practical reasons, this cluster expansion is truncated at some maximum cluster size. An effective vacancy diffusivity, $\overline{D_V}$, is then obtained by normalizing the total vacancy transport coefficient L_{VV} by the total vacancy concentration. The effect of clustering on vacancy transport can then be evaluated by comparing the $\overline{D_V}$ values obtained for different maximum cluster sizes. In the present work the maximum cluster size is successively increased to clusters containing 1, 2 and 3 solute atoms. Cluster analysis for dilute solute concentrations of 0.1 at.% and 0.5 at.%, see Figs. 4 and S2, shows that such small solute-vacancy clusters tend to contain only one vacancy, and the calculations of transport coefficients were thus restricted to clusters containing one vacancy. As illustrated in Fig. 9, the overall vacancy diffusion coefficient decreases as the initial solute concentration increases. For a fixed vacancy concentration of 10^{-5}, which is typical of the steady-state vacancy concentrations measured in our KMC simulations at 300 K, the overall vacancy diffusion coefficient $\overline{D_V}$ is significantly reduced when $[B]_{ini} > 0.1$ at.%, and this reduction is larger when larger maximum clusters are considered. For instance, for $[B]_{ini} = 0.1$ at.%, $\overline{D_V}$ is reduced from $\approx 2.5\times10^{-19}$ m^2/s to $\approx 1.9\text{x}10^{-19}$ m^2/s to $\approx 1.5\text{x}10^{-19}$ m^2/s when comparing the case where trapping occurs only on isolated B atoms to the case where it can occur on solute clusters of size 2 and 3, see Fig. 9. A similar improvement is observed when keeping $[B]_{ini}$ constant but decreasing the temperature, see Fig. 10. The beneficial effect of clusters on solute drag is even more pronounced, as shown in Fig. 11: For $[B]_{ini} = 0.1$ at.%, the solute drag coefficient, defined here as L_{BV}/L_{BB}, is reduced at 300 K from ≈ 0.79 to ≈ 0.70 to ≈ 0.63 for maximum cluster sizes of 1, 2, and 3 solute atoms, respectively. It is, unfortunately, not realistic to use KineCluE for larger solute concentrations and larger clusters, because in a physical sample the trajectories of vacancies kinetically bound to such clusters would be modified by the presence of other clusters, and thus the local equilibrium approximation would break down. Nevertheless, this case of $[B]_{ini} = 0.1$ at.% well illustrates the value of solute clustering. Lastly, it is worth noting that at temperatures above ≈ 500 K the drag ratios in Fig. 11 change sign, from positive to negative, indicative of inverse Kirkendall effect. As announced in the Section 2.1, such a transition temperature is consistent with the solute drag criterion $E_o - E_4 \gtrsim 3k_BT$ identified in ref. [17].

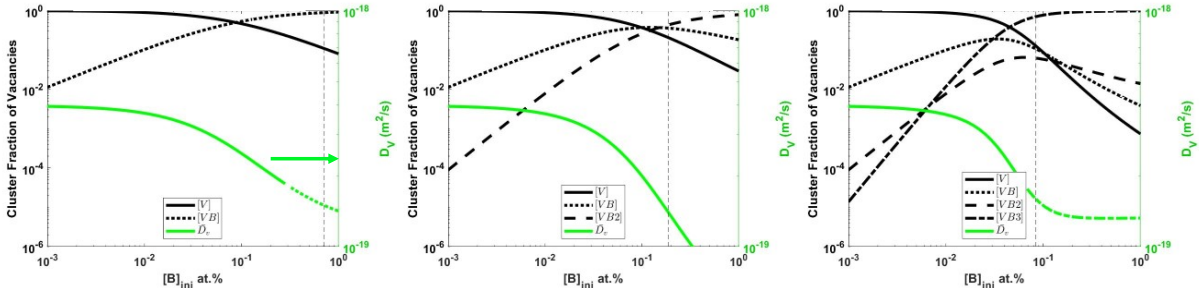

Figure 9. KineCluE calculations quantifying the effect of solute cluster on reducing the average vacancy diffusion coefficient $\overline{D_V}$, see definition in Eq. 7 in ref. [22]. The concentrations of free vacancies, [V], and bound vacancies [VB] and [VB2] are plotted (left y-axis) as a function of the B initial concentration $[B]_{ini}$. The resulting $\overline{D_V}$ is plotted in color (right y-axis) for T=300 K and [V]tot= 10^{-5}. The line style indicates the dominant contribution to the vacancy diffusion, corresponding to the concentration plots (black). The left figure corresponds to calculations with VB clusters only, the middle figure includes VB and VB2 clusters, while the right includes VB, VB2, and VB3 clusters. The vertical lines in each plot represent an estimate of the solute concentration above which the low-temperature expansion breaks down and results become untrustworthy.

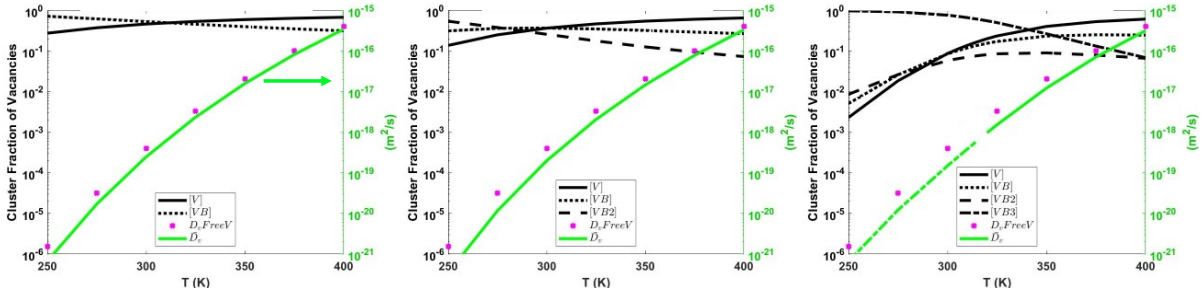

Figure 10. Same as in Fig. 9 but here varying the temperature while keeping constant the initial solute concentration at $[B]_{ini}$=0.1 at.%. Because the relative trapping strength of clusters is a function of temperature, the cluster dominating vacancy transport may change with temperature as well as with the clusters accounted for. The magenta datapoints are the transport coefficient of free, unbound vacancies.

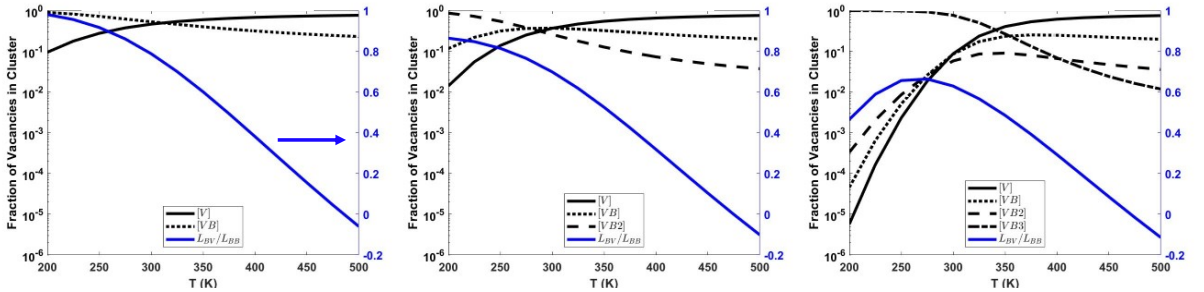

Figure 11. Same as in Fig. 10, but here plotting drag ratios, indicating the flux coupling between vacancies and solute. Note that the inclusion of VB_3 clusters leads to the prediction that the drag ratio will peak around 260 K, where the fraction of vacancies in clusters other than VB_3 become less than ≈1%. This behavior is significantly different than that predicted by only including VB and VB_2 clusters.

4 DISCUSSION

The primary finding of the present work is that the benefits of solute additions for trapping vacancies and promoting recombination are highly non-linear in solute concentration when solute clustering is significant. The atomistic simulations carried out in this work make it possible to quantify these effects and elucidate their atomistic origins. The increase in trapping strength is intimately related to the model used to calculate the energy of various solute-vacancy clusters. Here a pairwise interaction model that considers only first nearest-neighbor interactions was employed, resulting in a binding energy between a vacancy and a solute cluster that increases linearly with the number of solute atoms that are a first nearest neighbor of that vacancy. As the vacancy escape rate from a cluster is thermally activated, the resulting effects can be very large, and it is therefore important to evaluate the validity of our binding energy model. Since the model alloy is parametrized on Cu-Ag for the dilute range, the well-calibrated empirical interatomic potential for Cu-Ag by Williams et al [34] was used to calculate the binding energy of a vacancy to *n* Ag first nearest neighbors. This was done using LAMMPS (http://lammps.sandia.gov) [51] by relaxing relevant configurations with the above Cu-Ag interatomic potential for *n* up to 3. The

VAg_n binding energies are found to be 0.166, 0.332, and 0.551 eV respectively. These binding energies therefore increase nearly linearly with *n*, thus supporting the size-dependency of binding energies in the present pairwise interaction parametrization. For simulations specific to a particular alloy system, a more quantitative parametrization could be achieved using effective cluster interactions obtained from DFT calculations to determine the configuration energies required for KMC simulations, see for instance [52-54]. We also note that as the solute cluster size increases, fluctuations in the cluster shape would also contribute to vacancy trapping and escape rates.

A second important finding of this work is the value of solute clustering in suppressing solute drag, as illustrated by KineCluE calculations shown in Fig. 11. This effect, however, is more complex, resulting from kinetic correlations between the migration paths of vacancy and solute clusters. In the case of vacancy trapping on a single solute, for a given binding energy, the sign of the drag is only a function of w_1 and w_3 jump frequencies in the five-frequency model [55]. In contrast, for a vacancy trapped on a cluster with *n* solute atoms, many more frequencies will contribute to the drag coefficient. For small clusters, solute drag and cluster mobility can be calculated in a computationally efficient manner using KineCluE as done here and in ref. [56]. For larger clusters, the number of distinct configurations and jump frequencies to consider increase very quickly, and it may become preferrable to employ KMC simulations, see for instance refs. [27, 52, 57].

An unexpected result of this work is the observation that irradiation, even in the absence of direct A-B ballistic mixing, can shift the steady-state solubility limit to values larger than the equilibrium solubilities, as discussed in section 3.5 and illustrated in Figs. 4-7. Martin and Cauvin [58-61] had previously identified that recombination could affect solute solubility under irradiation, but with the opposite outcome, i.e., if solute atoms trap vacancies as in our Cu-Ag system, the steady state solubilities under irradiation can only be smaller than those in equilibrium. In this case irradiation induces homogeneous precipitation in undersaturated solid solutions, as observed for instance in Al-Zn [59]. We note, however, that the Cauvin-Martin model assumed that the solute-point defect binding energy was small compared to the solute-solute interaction, so that the solute cluster size distribution was unaffected by the point defect population. This assumption is not valid in our work as the solute-vacancy binding is in fact larger than the solute-solute interaction, and the solute cluster distribution is clearly modified by the presence of point defects, as seen in Figs. 4-6. The model of Maydet and Russell [62] and the recent model by Nastar et al. [63], on the other hand, do predict that in some cases irradiation could increase the solubility limit, but these models do not apply here since they rely on the relaxation of the elastic strain energy associated with the elimination of point defects and the formation of coherent [62] or semi-coherent [63] precipitates, while strain effects are ignored here.

One explanation for an increased solubility under irradiation considers the importance of the large binding energy between vacancy and solute atoms. Schuler et al. [64], for example, used first-principles calculations and KineCluE to demonstrate that in Fe-X alloys with X = O, N, C the strong binding energies between vacancies and the X interstitial species, 1.43 eV, 0.73 eV and 0.41 eV for X = O, N, C, respectively, can dramatically increase the low temperature solubility limit in these systems for typical steady-state vacancy concentrations under irradiation, i.e., $\approx 10^{-10}$ to 10^{-4}. The mechanism responsible for suppressing solute precipitation was labeled "vacancy-induced precipitate dissolution" (VID) since stable point defect-solute clusters stabilize solute atoms in the solid solution at the expense of solute precipitates [64]. A second possible explanation

is that the irreversible nature of recombination may modify the stability of clusters, i.e., when a vacancy initially trapped on a solute cluster disappears due its recombination with an interstitial solvent atom.

A first indication that the present shift in solubility is distinct from the VID mechanism identified by Schuler et al. [64] is that the cluster size distributions obtained from the full KMC simulations, see Fig. 12, do not match the ones expected from a local equilibrium approximation using a low-temperature expansion, which is assumed in the above reference for the VID mechanism. Indeed, while the cluster distributions agree fairly well for clusters that do not include vacancies, the VB_n clusters in the KMC simulations are much smaller than the ones expected from the low-temperature expansion calculations (note: sizes greater than n=5 have been excluded due to computing limitations, but this does not affect the main conclusion). Since the local equilibrium approximation is at the core of the VID mechanism, that mechanism is not valid here. A second indication that the solubility shift observed in the KMC simulations originates from a very different mechanism is that the steady-state cluster size distributions vary with displacement rates, as we now show.

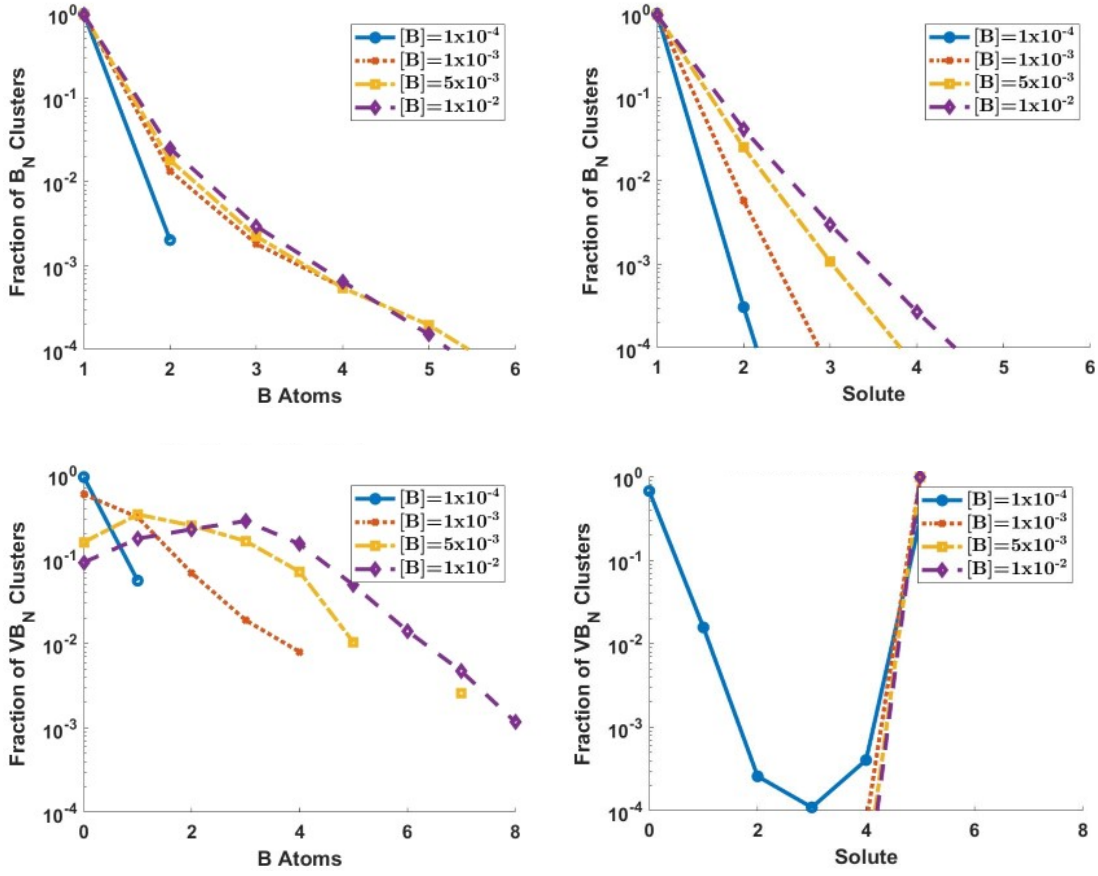

Figure 12. Size distributions of clusters with only solute (top row), and only one vacancy (bottom row) respectively. The system size is $128^2 \times 152$, and the temperature 300K. The figures on the left are from full KMC results, and the right are distributions predicted by KineCluE calculations of partition functions. The KMC results are averaged over the steady-state, and only considering the 'interior' half of the simulations, away from the sinks. The KineCluE calculations are performed with the vacancy and solute concentrations of the interior KMC results so that the results can be compared.

The role played by recombination on cluster distributions was directly addressed by performing, separate KMC simulations where the only modifications compared to the full simulations were (1) to turn off point defect elimination on the sink plane so that point defects created by irradiation can be eliminated only by recombination, and (2) to start the simulations with a non-zero number of pre-existing vacancies. In this case, keeping the irradiation temperature unchanged but varying the displacement rate from 10^{-7} to 10^{-4} dpa/s, leads to the steady-state solute cluster distribution changing dramatically, with much smaller clusters at the higher displacement rates, see Fig. 13. At the same time, the steady-state vacancy concentration in these simulations is virtually independent of the displacement rate because its value is dominated by the pre-existing vacancies (owing to the fast interstitial recombining immediately after production of a Frenkel pair, as described below). Specifically, a single vacancy was introduced prior to starting the irradiation simulation, thus translating to a background vacancy concentration of $\approx 4.0\times10^{-7}$, which, for the parameters used here, is much larger than the steady-state vacancy concentration due to irradiation in a microstructure without sinks. As the vacancy concentration is nearly constant, the solubility shift and the cluster size distributions expected from the VID mechanism should be independent of the displacement rate [64], but this is in direct contradiction with the KMC results shown in Fig. 13. It is therefore concluded that the solubility shift observed in these simulations that exclude sinks, as well as in the full KMC simulations discussed in Section 3, is driven by recombination. In regards to radiation resistance, this effect on solubility is highly beneficial because once precipitation takes place vacancy trapping is likely to saturate since, for a given solute concentration, a few large precipitates constitute a less effective trapping microstructure than many small solute clusters. From a more fundamental consideration, this finding represents a novel irradiation effect on phase stability. It mirrors the homogeneous radiation-induced precipitation reactions reported decades ago by Cauvin and Martin [58-61], but here shifting the solubility limit to values *higher* than the thermodynamic equilibrium solubility, instead of shifting it to *lower* values as in Cauvin and Martin's work.

Although there is no theory yet developed to quantify this new effect of recombination on solubility, it is clear that the net result of a recombination event in our system is to replace a vacancy trapped in a vacancy-solute cluster by a solvent atom, thus raising the energy of that cluster and suppressing its stability. One can make an analogy with the effects of ballistic mixing, but here extended to point defects. Indeed, for the no-sink simulation results presented in the previous paragraph, and in Fig. 13, the number of point defects in the simulation cell is either one vacancy and zero interstitials, or two vacancies and one interstitial. Recall, one vacancy was introduced in the cell prior to starting irradiation and isolated Frenkel pairs are created one at a time, at a rate controlled by the displacement rate. For the displacement rates and the simulation cell sizes investigated here, the high mobility of the interstitial leads to a recombination event before another Frenkel pair is created and before the vacancies can perform even one jump. If the interstitial recombines with the vacancy that was produced simultaneously with this interstitial, at site *j*, there is no net change in the system configuration. If the interstitial recombines with the other (pre-existing) vacancy, say at site *i*, the net result is a relocation of a vacancy from site *i* to site *j*, and corresponding change in local concentrations. This is therefore analogous to a ballistic relocation event for the vacancy, with an arbitrary large relocation distance. For the case of chemical mixing, arbitrary length ballistic relocations are known to be very effective in randomizing atomic configuration [65]. Moreover, short-range to finite-range ballistic mixing

events between vacancies and solute atoms have been shown in KMC simulations [66] and in KineCluE calculations [67] to result in a reduced, effective, vacancy-solute attraction. Furthermore, it is worth noting that, for alloys with attractive vacancy-solute interactions, these "ballistic" relocations of vacancies introduce a bias in the evolution of solute clusters: Since vacancies are trapped on solute clusters for most of their lifetime, vacancy-solvent ballistic relocations induce a net ballistic flux of vacancies from the clusters to the matrix. It is therefore not surprising that these relocations suppress the growth of the clusters. Nevertheless, it is intriguing to observe that this "forced mixing" of vacancies results in a new steady-state distribution for the solute clusters, shifted to smaller sizes compared to the equilibrium distribution. This shift suggests that irradiation, for the parameters considered in this study, can increase the solute solubility limit. From the above analysis, one concludes that this shift in solubility should be more noticeable as the displacement rate increases, although for the parameters used in the present KMC study, its manifestation is already clear for the relatively low displacement rate of 10^{-6} dpa/s. Further work is still needed to more formally describe this irradiation-induced increase in solubility.

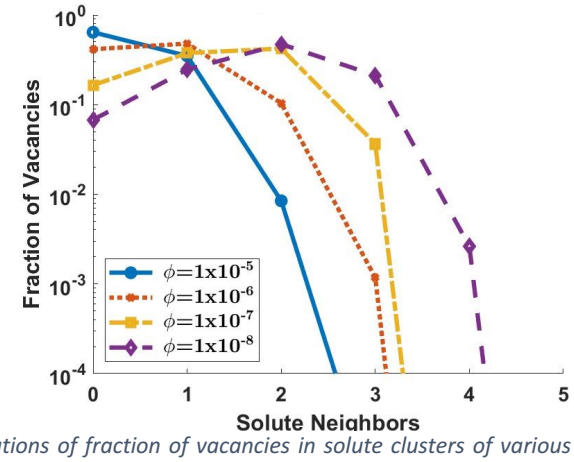

Figure 13. Steady-state distributions of fraction of vacancies in solute clusters of various sizes for simulations run with defect production at the indicated displacement rate (dpa/s) but no sinks. The initial solute concentration is 0.5 at.%. The system size is $128^2 \times 152$, and the temperature 300K. Note that the steady-state distribution shifts to smaller clusters as the damage rate increases.

In future work, it would be interesting to extend the present results by relaxing some of the constraints imposed here. In particular, we employed a sink boundary condition that resulted in solute segregation near the sink, see Fig. 1(a), which resulted in a thermal solute back flux large enough to maintain a non-zero solute concentration in the center of the simulation cell, far from the sinks. This setting is representative of the case where solute segregates uniformly all along the grain boundaries. An alternative boundary condition would be to remove solute atoms when they reach the sink. This setting, which would significantly increase the removal rate of the solute atoms from the system, would be more suitable for the case where solute segregation leads to precipitation at grain boundaries, with fast solute diffusion along the grain boundary feeding large precipitates located, for instance, at triple junctions. The effects reported in the present study should still be present, but as transient phenomena instead of stationary ones. Second, the KMC model prevents vacancy clustering, but this constraint is only physically acceptable if the V-clusters do not interact much with the solute concentration field, for instance because they are fast

diffusers and are removed at sinks fairly quickly compared to isolated vacancies. Third, direct A-B ballistic mixing was also ignored in the present study. Estimation of the ratio of the ballistic diffusion coefficient, D_b, to the radiation-enhanced thermal diffusion of vacancies, D_{th}^{irr}, suggests that this simplification is valid when the irradiation temperature exceeds ≈ 250-300 K for pure Cu and $\phi = 10^{-6}$ dpa/s. However, once trapping solute is added, D_{th}^{irr} decreases and in turn the relative importance of ballistic mixing effects is increased. Ballistic mixing would in fact act in the same direction as the recombination-induced precipitate dissolution identified here, further contributing to the destabilization of large solute clusters. Some amount of ballistic mixing could thus be beneficial too, provided that D_b is not so large that it would eliminate vacancy trapping on solute atoms and small clusters. Lastly, it would be interesting to extend this type of study to alloys where solute species, unlike in the Cu-Ag system, couple with interstitials as for instance in the Fe-based alloys studied by Schuler et al. [64]. In this regard, Krasnochtchekov et al. [68] investigated in model alloys how this coupling could induce solute clustering and precipitation.

5 CONCLUSION

The effects of adding solute atoms that trap vacancies on promoting point-defect recombination, and thus radiation resistance, have been investigated by kinetic Monte Carlo simulations for a model alloy based on Cu-Ag. It is found that increasing the solute concentration increases trapping and thus promotes radiation resistance, as anticipated, but that that improvement depends on the solute concentration in a highly non-linear manner. At high enough solute concentration, above ≈ 0.5 at % at 300 K in this model alloy, a dramatic increase in recombination rate and thus in radiation resistance is observed. This effect is triggered by the strong trapping of vacancies on solute clusters. The solute clustering is also observed to reduce solute drag and thus helps in retaining solute atoms in the grain interiors. Detailed analysis of the steady-state cluster size distributions for various irradiation damage rates establishes that these distributions deviate from those expected when clusters are in local equilibrium with their surroundings. It is shown that the irreversible character of the recombination reaction is at the origin of this effect, resulting in smaller but more numerous solute clusters, effectively shifting the solubility limit under irradiation to higher solute concentration. This solubility shift represents a novel kind of recombination-controlled phase transition similar to the homogeneous radiation-induced precipitation reactions observed for instance in Al-Zn and related systems but with an opposite sign.

Acknowledgments
This research is supported by the NSF under Grant No. DMR-1709857. We gratefully acknowledge stimulating discussions Dr. Thomas Schuler. This work made use of the Illinois Campus Cluster, a computing resource that is operated by the Illinois Campus Cluster Program (ICCP) in conjunction with the National Center for Supercomputing Applications (NCSA) and which is supported by funds from the University of Illinois at Urbana-Champaign.

Declaration of Interests

The authors declare that they have no known competing financial interests or personal relationships that could have appeared to influence the work reported in this paper.

APPENDIX A. THERMODYNAMIC AND KINETIC MODEL PARAMETERS

The broken bonds model used is described in the text, but here we define the equations relating the setting parameters to the interaction energies and saddle points used in our modified Cu-Ag system. The five-frequency model jumps expressed in the broken bonds format yield the following relationships.

$$E_0 = S_0 - 11\varepsilon_{AA} - 12\varepsilon_{AV}$$
$$E_1 = S_1 - 10\varepsilon_{AA} - 11\varepsilon_{AV} - \varepsilon_{AB} - \varepsilon_{BV}$$
$$E_2 = S_2 - 11\varepsilon_{AV} - 11\varepsilon_{AB} - \varepsilon_{BV}$$
$$E_3 = S_{3,4} - 11\varepsilon_{AA} - 11\varepsilon_{AV} - \varepsilon_{BV}$$
$$E_4 = S_{3,4} - 10\varepsilon_{AA} - 12\varepsilon_{AV} - \varepsilon_{AB}$$

The additional materials inputs of cohesive energy, vacancy formation energy, and heat of mixing are defined in terms of interaction energies below.

$$E_{coh}^{A} = \frac{Z}{2} * \varepsilon_{AA}$$
$$E_{coh}^{B} = \frac{Z}{2} * \varepsilon_{BB} = E_{coh}^{A} * \frac{T_m^B}{T_m^A}$$
$$E_{Vf}^{A} = Z * \varepsilon_{AV} - \frac{Z}{2} * \varepsilon_{AA}$$
$$w_{AB} = 2 * \varepsilon_{AB} - \varepsilon_{AA} - \varepsilon_{BB}$$
$$T_c * k_B = \frac{3w_{AB}}{12K_c}$$
$$K_c = 0.102069$$

Further discussion of this model can be found in ref. [69]

As this model only accounts for 1st NN interactions, the binding energy of the solute and vacancy at larger distances is neglected. This simplification is supported by comparison to the energetics defined by an interatomic potential developed for molecular dynamics simulations of Cu-Ag systems by Williams, Mishin, and Hamilton [34]. A large system (≈3,200 atoms) with a single vacancy and single Ag atom was allowed to relax in various configurations, and the vacancy-Ag binding energy calculated from the differences in system energy. This showed that while the 1st NN binding was significant 0.166 eV, the 2nd, 3rd, and 4th NN binding energies were small, being just -0.024 eV, -0.013 eV, and 0.007 eV respectively. These results thus justify our simplification to only consider 1st NN interactions. While the system of equations above is parameterized using a single vacancy and a single solute, here we assess the accuracy of the energetics model for a larger cluster. We prepared another parameterization based on the Williams-Mishin-Hamilton Cu-Ag potential. The interaction parameters are defined based on relaxed configuration energies and the parameterization scheme given in ref. [70]. The saddle point energies were fit using the 5-frequency energy barriers calculated for this potential using NEB as implemented in LAMMPS. These new parameters were applied to the KMC scheme, and the results compared to the LAMMPS-calculated migration energy barriers for a cluster with a vacancy and two solutes. The results are shown in Fig. A1.

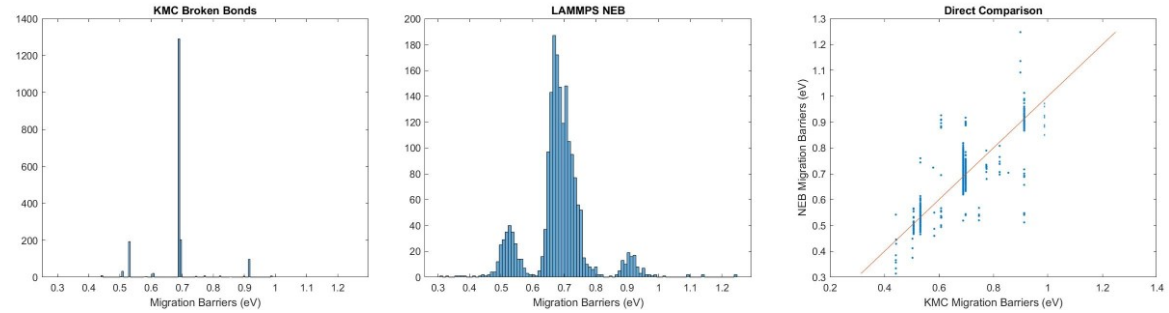

Figure A1. The histograms of migration energies relevant to the VB_2 cluster using the Williams-Mishin-Hamilton EAM potential for Cu-Ag. The migration energies are calculated as (a) a KMC parameterization from the potential and (b) using NEB calculations. Individual jump comparisons are shown as a scatter plot in (c).

These plots show that the main features of the migration energy histogram are captured by the KMC scheme, despite the significant scatter for specific jumps that can be shown by the jump-by-jump comparison shown in Fig. A1(c). This loss of accuracy is a trade-off made with the significant simplification of the energetics scheme, including the ability to calculate barriers for arbitrary configurations without running NEB calculations.

As indicated in Section 2.3, for a given system size in the KMC simulations, different sink strengths can be deduced because of the change in recombination fraction with increasing the solute concentration. Sink strength values corresponding to the systems sizes used in the simulations have been calculated using the geometric model of Damask and Dienes [40], which does not account for recombination and those values are thus independent of composition; and using the approach of Doan and Martin [43], which does include recombination, and thus leading to sink strength values that depend on the alloy composition.

Table A3 Calculated sink strengths of the systems, using a geometric expression and the Doan & Martin (D&M) method for A-B alloys with solute concentrations of 0.0, 0.1, 1.0 and 2.0 at%. Calculations are made with values averaged over the whole simulation time. Sink strength values are given in units of m^{-2}.

Planes	Geometric model (π^2/t^2)	D&M (0.0 at.%)	D&M (0.1 at.%)	D&M (1 at.%)	D&M (2 at.%)
48	$9.81\text{x}10^{16}$	$1.08\text{x}10^{17}$	$9.14\text{x}10^{16}$	$1.80\text{x}10^{16}$	$1.11\text{x}10^{16}$
86	$3.05\text{x}10^{16}$	$4.11\text{x}10^{16}$	$3.42\text{x}10^{16}$	$9.02\text{x}10^{15}$	$5.77\text{x}10^{15}$
152	$9.78\text{x}10^{15}$	$1.87\text{x}10^{16}$	$1.52\text{x}10^{16}$	$4.89\text{x}10^{15}$	$3.32\text{x}10^{15}$

APPENDIX B. CONTINUUM MODEL FOR SOLUTE SEGREGATION IN IRRADIATED INFINITELY DILUTE ALLOYS.

We recall here the main points of the continuum model introduced in ref. [17] for infinitely dilute alloys with vacancy-trapping solute. The system is decomposed into a homogeneous bulk part and

a sink region. The bulk region is assumed to be a dilute ideal solid solution and solute-vacancy pair concentrations are determined from a low-temperature local equilibrium approximation. The segregation of solute onto the sink results from solute drag to the sink due to solute-vacancy coupled fluxes, partly compensated by a thermodynamic back flux of solute from the sink to the bulk. For the solute drag term, vacancy and solute transport coefficients are calculated using the self-consistent mean field (SCMF) method [18-20, 71], as implemented in the KineCluE code [21] considering transport by either free vacancies or complexes comprised of one vacancy and one solute. Two modifications were made in this work compared to ref. [17], in order to match the conditions used in the KMC simulations. The first modification relates to the back flux, which is proportional to the vacancy concentration immediately adjacent to the sink. That concentration was set to be equal to its bulk equilibrium value in ref. [17], resulting in a negligible back flux and thus in the progressive removal of nearly all the solute from the bulk. That boundary vacancy concentration just outside of the sink is in fact affected by supersaturation of vacancies resulting from irradiation, and here we determine this value using approximate solutions for steady-state point defect concentration in a unary system under irradiation, using Eqs. (50-51) in ref. [72]. The vacancy concentration is evaluated at a distance corresponding to one (111) atomic plane away from the sink and, for simplicity, all parameters are taken from the data used for the A species in the KMC simulations. This new vacancy concentration just outside of the sink is significantly higher than the equilibrium value, leading to a finite solute back flux and thus a non-zero steady-state solute concentration in the bulk. The second and minor modification is that we initialized the sink region with the initial solute concentration, instead of zero solute as in ref. [17].

It is seen from Fig. 2 and Fig. B1 that the agreement between the KMC results and the continuum kinetic model is very good *for dilute alloys*, e.g., 0.01 and 0.1 at.% initial solute concentrations. While the KMC results are noisier due to the stochastic nature of the simulation, the steady-state sink solute concentrations and averaged F_R match well. In addition, the characteristic time scales for reaching steady state in the KMC simulations are also in good agreement with those predicted by the continuum model. We note that while the continuum model is initialized with an assumed vacancy concentration, the vacancy concentration in the KMC simulations needs to be built up from defect production. This can lead to a transient with lower F_R, which is strongly dependent on vacancy concentration. We also note that solute is dragged to the sink during this transient, reducing the expected vacancy concentration enhancement due to trapping. While this transient may be seen in the KMC results for the 0.5 at.% initial solute concentration, for lower concentrations this transient is short enough to be practically undetectable for our system parameters.

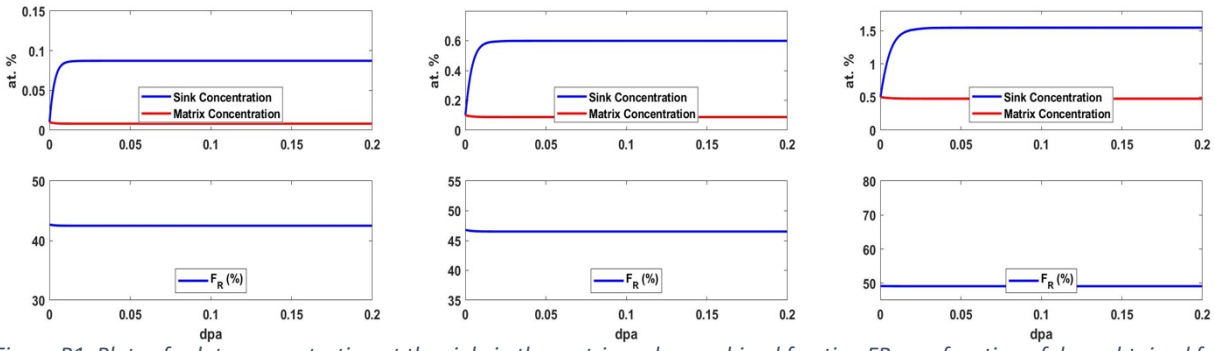

Figure B1. Plots of solute concentration at the sink, in the matrix and recombined fraction FR as a function of dose obtained from the Continuum Model for a dilute Cu-Ag alloy. Sink strength is k^2=4.0x10^{16} m^{-2}, i.e., the value for pure Cu for a system size of

128^2x86 sites (using Doan & Martin's expression); displacement rate $\phi = 10^{-6}$ dpa/s, T=300K, and Ag concentration is 0.01 at.% (Left), 0.1 at.% (Center), and 0.5 at.% (Right).

REFERENCES

1. Zinkle, S.J. and G.S. Was, *Materials challenges in nuclear energy.* Acta Materialia, 2013. **61**(3): p. 735-758.
2. Nastar, M. and F. Soisson, *1.08 - Radiation-Induced Segregation ☆*, in *Comprehensive Nuclear Materials (Second Edition)*, R.J.M. Konings and R.E. Stoller, Editors. 2020, Elsevier: Oxford. p. 235-264.
3. Ardell, A.J. and P. Bellon, *Radiation-induced solute segregation in metallic alloys.* Current Opinion in Solid State and Materials Science, 2016. **20**(3): p. 115-139.
4. Odette, G.R., M.J. Alinger, and B.D. Wirth, *Recent developments in irradiation-resistant steels*, in *Annual Review of Materials Research*, D.R. Clarke, M. Ruehle, and A.P. Tomsia, Editors. 2008. p. 471-503.
5. Koehler, J.S., *Decrease in Void Growth-Rate by Interstitial Trapping.* Journal of Applied Physics, 1975. **46**(6): p. 2423-2428.
6. Mansur, L.K. and M.H. Yoo, *Effects of Impurity Trapping on Irradiation-Induced Swelling and Creep.* Journal of Nuclear Materials, 1978. **74**(2): p. 228-241.
7. Mansur, L.K., *Effects of Point-Defect Trapping and Solute Segregation on Irradiation-Induced Swelling and Creep.* Journal of Nuclear Materials, 1979. **83**(1): p. 109-127.
8. Demkowicz, M.J., R.G. Hoagland, and J.P. Hirth, *Interface structure and radiation damage resistance in Cu-Nb multilayer nanocomposites.* Physical Review Letters, 2008. **100**(13): p. 136102.
9. Hattar, K., et al., *Arrest of He bubble growth in Cu-Nb multilayer nanocomposites.* Scripta Materialia, 2008. **58**(7): p. 541-544.
10. Beyerlein, I.J., et al., *Radiation damage tolerant nanomaterials.* Materials Today, 2013. **16**(11): p. 443-449.
11. Kato, T., H. Takahashi, and M. Izumiya, *Effects of systematic modification with oversized elements on void formation in 316L austenitic stainless steel under electron irradiation.* Materials Transactions, JIM, 1991. **32**(10): p. 921-930.
12. Sakaguchi, N., S. Watanabe, and H. Takahashi, *Effect of additional minor element on radiation-induced grain boundary segregation in austenitic stainless steel under electron irradiation.* Proceedings of the 1998 4th International Conference on Computer Simulation of Radiation Effects in Solids (COSIRES), 1999. **153**(1-4): p. 142-146.
13. Hackett, M.J., et al., *Effects of oversized solutes on radiation-induced segregation in austenitic stainless steels.* Journal of Nuclear Materials, 2009. **389**(2): p. 265-278.
14. Hackett, M.J., R. Najafabadi, and G.S. Was, *Modeling solute-vacancy trapping at oversized solutes and its effect on radiation-induced segregation in Fe-Cr-Ni alloys.* Journal of Nuclear Materials, 2009. **389**(2): p. 279-287.
15. Kato, T., et al., *The effect of solute content on grain boundary segregation in electron-irradiated Fe-Cr-Mn alloys.* Journal of Nuclear Materials, 1991. **179-181**(PART 1): p. 623-625.

16. Kato, T., H. Takahashi, and M. Izumiya, *Grain boundary segregation under electron irradiation in austenitic stainless steels modified with oversized elements.* Journal of Nuclear Materials, 1992. **189**(2): p. 167-174.
17. Schuler, T., et al., *Modeling the long-term evolution of dilute solid solutions in the presence of vacancy fluxes.* Physical Review Materials, 2018. **2**(7).
18. Nastar, M., V.Y. Dobretsov, and G. Martin, *Self-consistent formulation of configurational kinetics close to equilibrium: the phenomenological coefficients for diffusion in crystalline solids.* Philosophical Magazine a-Physics of Condensed Matter Structure Defects and Mechanical Properties, 2000. **80**(1): p. 155-184.
19. Nastar, M., *A mean field theory for diffusion in a dilute multi-component alloy: a new model for the effect of solutes on self-diffusion.* Philosophical Magazine, 2005. **85**(32): p. 3767-3794.
20. Nastar, M. and V. Barbe, *A self-consistent mean field theory for diffusion in alloys.* Faraday Discussions, 2007. **134**: p. 331-342.
21. Schuler, T., L. Messina, and M. Nastar, *KineCluE: A kinetic cluster expansion code to compute transport coefficients beyond the dilute limit.* Computational Materials Science, 2020. **172**: p. 109191.
22. Schuler, T., et al., *Design principles for radiation-resistant solid solutions.* Physical Review B, 2017. **95**(17).
23. Daniels, C. and P. Bellon, *Hybrid kinetic Monte Carlo algorithm for strongly trapping alloy systems.* Computational Materials Science, 2020. **173**: p. 109386.
24. Bonny, G., et al., *The impact of alloying elements on the precipitation stability and kinetics in iron based alloys: An atomistic study.* Computational Materials Science, 2019. **161**: p. 309-320.
25. Zhang, S., et al., *Self healing of radiation-induced damage in Fe–Au and Fe–Cu alloys: Combining positron annihilation spectroscopy with TEM and ab initio calculations.* Journal of Alloys and Compounds, 2020. **817**.
26. Binder, K. and D. Stauffer, *Theory for the slowing down of the relaxation and spinodal decomposition of binary mixtures.* Physical Review Letters, 1974. **33**(17): p. 1006-1009.
27. Le Bouar, Y. and F. Soisson, *Kinetic pathways from embedded-atom-method potentials: Influence of the activation barriers.* Physical Review B - Condensed Matter and Materials Physics, 2002. **65**(9): p. 941031-9410314.
28. Soisson, F., *Kinetic Monte Carlo simulations of radiation induced segregation and precipitation.* Journal of Nuclear Materials, 2006. **349**(3): p. 235-250.
29. Shu, S.P., P. Bellon, and R.S. Averback, *Role of point-defect sinks on irradiation-induced compositional patterning in model binary alloys.* Physical Review B, 2015. **91**(21): p. 214107.
30. Leclaire, A.D., *Theory of Impurity Diffusion in Metals.* Philosophical Magazine, 1962. **7**(73): p. 141-+.
31. Philibert, J., *Atom Movements: Diffusion and Mass Transport in Solids*. Monographies de physique. 1991, Les Ulis, France: Editions de Physique. 577.
32. Wu, H., T. Mayeshiba, and D. Morgan, *High-Throughput ab-initio dilute solute diffusion database.* Scientific Data, 2016. **3**: p. 160054.
33. Dane, M., M. Tam, and M. Dane, *DFT dilute solute diffusion in Al, Cu, Ni, Pd, Pt, Mg, and W*. 2016.
34. Williams, P.L., Y. Mishin, and J.C. Hamilton, *An embedded-atom potential for the Cu-Ag system.* Modelling and Simulation in Materials Science and Engineering, 2006. **14**(5): p. 817-833.
35. Lu, H.J., et al., *First-principles investigation on diffusion mechanism of alloying elements in dilute Zr alloys.* Acta Materialia, 2018. **154**: p. 161-171.
36. Messina, L., et al., *Solute diffusion by self-interstitial defects and radiation-induced segregation in ferritic Fe-X (X=Cr, Cu, Mn, Ni, P, Si) dilute alloys.* Acta Materialia, 2020. **191**: p. 166-185.

37. Tendler, R. and J.P. Abriata, *Atomic Size and Fast Diffusion of Metallic Impurities in Zirconium.* Journal of Nuclear Materials, 1987. **150**(3): p. 251-258.
38. Rehn, L.E. and P.R. Okamoto, *Non-equilibrium segregation in irradiated alloys*, in *Phase Transformations during Irradiation*, F.V. Nolfi, Editor. 1983, Applied Science Publishers Ltd: Barking (UK). p. 247-290.
39. Duesing, G., et al. *The influence of spontaneous recombinations and sub-threshold events on the defect production at low temperature electron irradiations*. in *Int. Conf. on Vacancies and Interstitials in Metals*. 1967. Juelich, Germany: North-Holland Publ. Co, Amsterdam.
40. Damask, A.C. and G.J. Dienes, *Point Defects in Metals*. 1972, New-York: Gordon & Breach.
41. Nichols, F.A., *On the estimation of sink-absorption terms in reaction-rate-theory analysis of radiation damage.* Journal of Nuclear Materials, 1978. **75**(1): p. 32-41.
42. Rauht, H., et al., *Void sink strength including bulk recombination.* Philosophical Magazine A: Physics of Condensed Matter, Structure, Defects and Mechanical Properties, 1981. **44**(6): p. 1255-1276.
43. Doan, N.V. and G. Martin, *Elimination of irradiation point defects in crystalline solids: Sink strengths.* Physical Review B - Condensed Matter and Materials Physics, 2003. **67**(13).
44. Bortz, A.B., M.H. Kalos, and J.L. Lebowitz, *New Algorithm for Monte-Carlo Simulation of Ising Spin Systems.* Journal of Computational Physics, 1975. **17**(1): p. 10-18.
45. Mason, D.R., R.E. Rudd, and A.P. Sutton, *Stochastic kinetic Monte Carlo algorithms for long-range Hamiltonians.* Computer Physics Communications, 2004. **160**(2): p. 140-157.
46. Rehn, L.E., P.R. Okamoto, and R.S. Averback, *Relative efficiencies of different ions for producing freely migrating defects.* Physical Review B, 1984. **30**(6): p. 3073-3080.
47. Müller, A., V. Naundorf, and M.P. MacHt, *Point defect sinks in self-ion-irradiated nickel: A self-diffusion investigation.* Journal of Applied Physics, 1988. **64**(7): p. 3445-3455.
48. Fielitz, P., et al., *Atom transport in nickel by displacement cascades for spatially dependent displacement rate and sink strength.* Applied Physics Letters, 1996. **69**(3): p. 331-333.
49. Balluffi, R.W., S.M. Allen, and W.C. Carter, *Kinetics of Materials*. Kinetics of Materials. 2005: John Wiley and Sons. 1-645.
50. Cahn, J.W. and J.E. Hilliard, *Free energy of a nonuniform system. I. Interfacial free energy.* The Journal of Chemical Physics, 1958. **28**(2): p. 258-267.
51. Plimpton, S., *Fast parallel algorithms for short-range molecular dynamics.* Journal of Computational Physics, 1995. **117**(1): p. 1-19.
52. Soisson, F. and C.C. Fu, *Cu-precipitation kinetics in α-Fe from atomistic simulations: Vacancy-trapping effects and Cu-cluster mobility.* Physical Review B - Condensed Matter and Materials Physics, 2007. **76**(21).
53. Bhattacharya, J. and A. Van der Ven, *Phase stability and nondilute Li diffusion in spinel ${\text{Li}}_{1+x}{\text{Ti}}_{2}{\text{O}}_{4}$.* Physical Review B, 2010. **81**(10): p. 104304.
54. Li, C., et al., *Predicting activation energies for vacancy-mediated diffusion in alloys using a transition-state cluster expansion.* Physical Review Materials, 2021. **5**(1).
55. Philibert, J., *Atom movements : diffusion and mass transport in solids*. Monographies de physique. 1991, Les Ulis, France: Editions de Physique.
56. Schuler, T., M. Nastar, and L. Messina, *Mass-transport properties of ternary Fe(C,O) alloys revealed by multicomponent cluster synergies.* Physical Review Materials, 2020. **4**(2): p. 020401.
57. Pascuet, M.I., et al., *Stability and mobility of Cu-vacancy clusters in Fe-Cu alloys: A computational study based on the use of artificial neural networks for energy barrier calculations.* Journal of Nuclear Materials, 2011. **412**(1): p. 106-115.
58. Cauvin, R. and G. Martin, *Radiation induced homogeneous precipitation in undersaturated solid-solutions.* Journal of Nuclear Materials, 1979. **83**(1): p. 67-78.

59. Cauvin, R. and G. Martin, *Solid solutions under irradiation. II. Radiation-induced precipitation in AlZn undersaturated solid solutions.* Physical Review B, 1981. **23**(7): p. 3333-3348.
60. Cauvin, R. and G. Martin, *Solid solutions under irradiation. I. A model for radiation-induced metastability.* Physical Review B, 1981. **23**(7): p. 3322-3332.
61. Cauvin, R. and G. Martin, *Solid solutions under irradiation. iii. further comments on the computed solubility limit.* Physical Review B, 1982. **25**(5): p. 3385-3388.
62. Maydet, S.I. and K.C. Russell, *Precipitate stability under irradiation: Point defect effects.* Journal of Nuclear Materials, 1977. **64**(1-2): p. 101-114.
63. Nastar, M., et al., *Thermodynamic model for lattice point defect-mediated semi-coherent precipitation in alloys.* Communications Materials, 2021. **2**(1): p. 32.
64. Schuler, T., M. Nastar, and F. Soisson, *Vacancy-induced dissolution of precipitates in out-of-equilibrium systems: A test case of FeX (X= C,N,O) alloys.* Physical Review B, 2017. **95**(1).
65. A. Enrique, R. and P. Bellon, *Phase stability under irradiation in alloys with a positive heat of mixing: effective thermodynamics description.* Physical Review B - Condensed Matter and Materials Physics, 1999. **60**(21): p. 14649-14659.
66. Roussel, J.-M. and P. Bellon, *Self-diffusion and solute diffusion in alloys under irradiation: Influence of ballistic jumps.* Physical Review B, 2002. **65**(14): p. 144107.
67. Huang, L., T. Schuler, and M. Nastar, *Atomic-scale modeling of the thermodynamic and kinetic properties of dilute alloys driven by forced atomic relocations.* Physical Review B, 2019. **100**(22).
68. Krasnochtchekov, P., R.S. Averback, and P. Bellon, *Homogeneous phase separation in binary alloys under ion irradiation conditions: Role of interstitial atoms.* Physical Review B - Condensed Matter and Materials Physics, 2007. **75**(14).
69. Daniels, C. and P. Bellon, *Hybrid kinetic Monte Carlo algorithm for strongly trapping alloy systems.* Computational Materials Science, 2020. **173**.
70. Le Bouar, Y. and F. Soisson, *Kinetic pathways from embedded-atom-method potentials: Influence of the activation barriers.* Physical Review B, 2002. **65**(9).
71. Nastar, M., *Mean field kinetics: a sound framework for understanding diffusion in alloys.* Diffusions in Materials: Dimat2000, Pts 1 & 2, 2001. **194-1**: p. 171-182.
72. Sizmann, R., *The effect of radiation upon diffusion in metals.* Journal of Nuclear Materials, 1978. **69-70**(C): p. 386-412.